

Article

Experimental Studies on the Seismic Performance of Underwater Concrete Piers Strengthened by Self-Stressed Anti-Washout Concrete and Segments

Yu Sun ^{1,2,*}, Wansong Xu ^{1,3} and Sheng Shen ^{1,*}¹ College of Civil Engineering, Fuzhou University, Fuzhou 350108, China; ixuwansong@163.com² Shanghai Construction Decoration Engineering Group Co., Ltd., Shanghai 200040, China³ East China Electric Power Design Institute Co., Ltd. of China Power Engineering Consulting Group, Shanghai 200333, China

* Correspondence: sy1519446906@163.com (Y.S.); s_shen@fzu.edu.cn (S.S.); Tel.: +86-519-15189707365 (Y.S.); +86-591-18065157513 (S.S.)

Abstract: Given that the existing drainage strengthening methods for underwater damaged piers are expensive, inefficient, and cause shipping traffic disruptions, an urgent need exists to explore undrained strengthening methods, such as the precast concrete segment assembly method (PCSAM). However, the PCSAM has certain limitations, including a considerable strength loss of filled concrete, poor accuracy, poor connection performance of the segment sleeves, etc. Hence, this study developed an improved PCSAM (IPCSAM) by adopting self-stressed anti-washout concrete (SSAWC) as the filling material and developing a lining concrete segment sleeve (LCSS) based on the design principle of shield tunnel lining segments. Subsequently, the seismic performance of the strengthened piers was investigated. First, nine 1/5-scale pier column specimens were designed by considering different influencing factors: the self-stress of the SSAWC, LCSS reinforcement ratio, and initial damage and length–diameter ratio of the pier column. These specimens were tested under low reversed cyclic loading. Second, an extended parameter analysis was performed based on the established numerical models consistent with the quasi-static test’s parameter settings. Finally, a restoring force model of the strengthened piers, including the trilinear skeleton curve model and hysteresis curve model, was established based on the results of the quasi-static test and parameter analysis. The results indicated that the bearing capacity, ductility, and initial stiffness of the specimens strengthened using the IPCSAM increased by approximately 83.5–106.4%, 16.3–50.2%, and 83.9–177.3%, respectively, with the energy dissipation capacity also significantly improved. The self-stress of the SSAWC should not exceed 2.2 MPa, and the recommended ratio of the LCSS thickness to pier column diameter is 1/10. Additionally, the proposed restoring force model is highly accurate and applicable, able to provide a reference for the practical seismic strengthening design of piers.

Keywords: underwater concrete pier; seismic performance; self-stressed anti-washout concrete; segment assembly; undrained strengthening; quasi-static test



Citation: Sun, Y.; Xu, W.; Shen, S. Experimental Studies on the Seismic Performance of Underwater Concrete Piers Strengthened by Self-Stressed Anti-Washout Concrete and Segments. *Appl. Sci.* **2023**, *13*, 12034. <https://doi.org/10.3390/app132112034>

Academic Editor: Rosario Montuori

Received: 2 September 2023

Revised: 22 October 2023

Accepted: 24 October 2023

Published: 4 November 2023



Copyright: © 2023 by the authors. Licensee MDPI, Basel, Switzerland. This article is an open access article distributed under the terms and conditions of the Creative Commons Attribution (CC BY) license (<https://creativecommons.org/licenses/by/4.0/>).

1. Introduction

As essential elements of bridges for load transfer, substructural components, such as piers and piles, directly influence the structure’s safety, durability, and normal-use performance [1]. Due to previous low design code requirements, degradation of materials during the service period and environmental erosion have led to various types of damage, including cavities, spalling, and cracks on the surface of underwater piers, degeneration of the load-carrying capacity and seismic performance of bridges, and sudden collapse due to strong current impact [2,3]. Several seismic strengthening techniques are applied for existing bridge piers, including section enlargement [4,5], externally bonded steel plates [6], bar planting [4,7], outer sleeve reinforcement [8,9], fiber-reinforced polymer (FRP)

wrapping [10–13], wire wrapping [14], and extraneous prestressed strengthening [15–18]. Although these techniques have well-established design theories and excellent strengthening effects, they are expensive, inefficient, and cause shipping traffic disruptions due to the unavoidable construction of cofferdams for drainage before the strengthening work is implemented [2]. Consequently, undrained seismic strengthening methods have attracted increased interest over the past decade.

Recently, undrained seismic strengthening methods, including the jacket method [19,20], FRP underwater strengthening method [21–24], and precast concrete segment assembly method (PCSAM) [23], have been proposed and applied in practical engineering. Due to the omission of the water draining process, these methods are more economical, efficient, and shipping traffic-friendly. However, specific challenges remain. For instance, in the jacket method, glass fiber sleeves are used to wrap piers to improve their durability; however, this limits improvements in the mechanical properties of underwater piers and can cause strengthening failure when used to wrap piers in deep water [23]. In the FRP underwater strengthening method, the resin adhesive for bonding the FRP can degrade after immersion in water for a long time, leading to bond failure at the interface between the FRP and components [22]. In contrast, the PCSAM uses several precast concrete segments reinforced with basalt FRP grids to form a sleeve ring wrapping the pier via piecewise assembly; the sleeve is then tightened by prestressing high-strength wire ropes wound on the surface of the pier through customized anchorages; finally anti-washout underwater concrete (AWC) is poured into the interspace between the sleeve and pier to achieve undrained and deep-water strengthening [23,25]. As a prestressed strengthening technique, the PCSAM eliminates stress–strain hysteresis through active strengthening and enables the pier and strengthened aspect to work together, which can significantly improve the seismic performance of components by constraining the core concrete of piers with circumferential pressure. Nevertheless, the PCSAM has certain defects, including a large prestress loss and poor durability of the wire ropes, poor accuracy and connection performance of the sleeves, large strength loss of the filled concrete, and uncertain bonding properties between the filled concrete and segment sleeves [2].

To address these limitations, our research team has proposed an improved PCSAM (IPCSAM) [2], depicted in Figure 1. On the one hand, regarding the design theory and prefabrication technology of the shield tunnel lining segments, the connection of the reinforced segment sleeve is improved by a lining concrete segment sleeve (LCSS), owing to its high precision in prefabrication [26], good joint connection strength and connection effects [27], and good durability [28]. On the other hand, self-stressed anti-washout underwater concrete (SSAWC) is applied as a filling material between the pier column and LCSS to generate accurate initial self-stress inside the filling layer. That is, an additional appropriate expansion agent is used in the SSAWC instead of applying prestress on the outer surface of the pier using wire ropes. This has the following advantages: (a) Circumferential confining pressure is applied to improve the mechanical properties of concrete in the core pier column [2]. (b) The prestress and strength losses of filled concrete are reduced [1,29]. (c) The bonding strength between the filling layer and adjacent members is increased by reducing the shrinkage effect of the filled concrete [30].

Wu et al. [2] found that the axial compression performance of strengthened piers is effectively improved using the IPCSAM. However, the seismic performance of underwater concrete piers strengthened using the IPCSAM remains to be evaluated in depth. To achieve this, several factors influencing the seismic performance of the strengthened piers must be considered: (a) The thickness, concrete strength, and reinforcement ratio of the LCSS. Tang [23] proposed that increasing the reinforcement ratio of FRP bars embedded in concrete segments improves the seismic performance of strengthened bridge columns, indicating that a high LCSS reinforcement ratio might improve the seismic performance of strengthened piers. (b) The self-stress value, thickness, strength, and reinforcement ratio of the SSAWC. Huang et al. [31–34] found that setting an appropriate self-stress value can enhance the seismic performances of the concrete-filled steel tubular columns.

Moreover, Tang [35] reported that an excessive prestress level could reduce the columns' ultimate displacement and ductility. (c) Length–diameter ratio, axial compression ratio, and initial damage of the pier column. Deng et al. [36–41] reported that a high axial compression ratio of the pier column could reduce ductility and rapid stiffness degradation. Meanwhile, Fakharifar et al. [18,42,43] strengthened pier columns with varying degrees of initial damage using prestressed steel jackets and CFRP, restoring the seismic performance of damaged piers to intact conditions or better. Zhong [44] and Wang [45] found that the bearing capacity, ductility, and energy dissipation capacity decreased with an increase in the length–diameter ratio of concrete-filled steel tubular columns, indicating that a high length–diameter ratio might weaken the seismic performance of piers. The selection of these influencing factors is further discussed in Sections 2 and 4. Additionally, establishing a restoring force model is of great significance for the seismic design and elasto-plastic time-history analysis of underwater concrete piers. In particular, Deng et al. [46–50] proposed restoring force models of concrete-filled steel tubular columns under different working conditions.

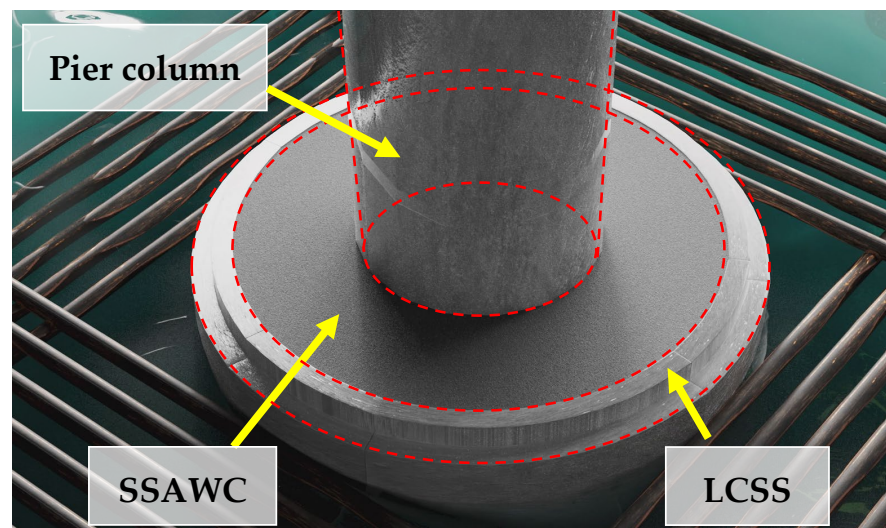


Figure 1. Schematic of the pier column strengthened using the IPCSAM. Note: SSAWC, self-stressed anti-washout underwater concrete; LCSS, lining concrete segment sleeve.

This study investigates the seismic performance of underwater concrete piers strengthened using the IPCSAM. As described in Sections 2 and 3, a total of nine 1/5-scale specimens were divided into three groups, in which influencing factors, such as the self-stress of the filled concrete, reinforcement ratio of the segment, and initial damage and length–diameter ratio of the pier column, were considered. The specimens were tested under cyclic horizontal loading to verify the seismic strengthening effect of the IPCSAM and analyze the influence of different factors on seismic performance. In Section 4, extended parameter analysis is presented using numerical simulations. In Section 5, the restoring force model of pier columns strengthened using the IPCSAM is established according to the results of the quasi-static test and extended parameter analysis, providing a theoretical basis for the seismic design of piers strengthened using the IPCSAM.

2. Experimental Program

2.1. Specimen Grouping and Design

The objective of this study was to investigate the effects of different influencing factors, including the self-stress of the filled concrete, reinforcement ratio of the segment, and initial damage and length–diameter ratio of the pier column, on the seismic performance of strengthened piers, and to verify the seismic strengthening effect of the IPCSAM. First, the test specimens were reasonably designed and grouped. An unreinforced core pier column, LCSS, and SSAWC were then designed for specimens strengthened using the IPCSAM.

2.1.1. Specimen Grouping and Comparison Setting

Four influencing factors, namely the self-stress, initial damage, length–diameter ratio, and reinforcement ratio of the LCSS, were set as the control variables of the specimens. The following were conducted for the other factors: (a) The thickness, strength, and reinforcement ratio of the filled concrete were not considered key control variables for the seismic performance of specimens because numerous studies [40,44,45,51–55] have analyzed the impact of these three common variables on the seismic performance of columns and reached similar conclusions; that is, the high reinforcement ratio of the filled concrete can significantly improve the bearing capacity and ductility of columns under low cyclic horizontal loads [44]. (b) Compared with the improved connection performance of the segment sleeve, the influence of the LCSS thickness and concrete strength on the seismic performance of piers was relatively small. The LCSS thickness remained constant due to the limitations of the prefabricated mold used for the segments. Hence, investigating only the effect of weakening the segment sleeve reinforcement ratio on the seismic performance is sufficient. (c) Considering the slight variation in the axial compression ratio during the loading process of the piers [2], the same axial compression ratio was adopted for all test specimens. Moreover, several variables, including the segment thickness, reinforcement ratio, filled concrete strength, and axial compression ratio of the pier column, were considered in subsequent numerical simulations for the extended parameter analysis.

As shown in Table 1, the nine specimens were divided into three groups (G0, G1, and G2) based on the experimental objectives. The test control group (G0) included three unreinforced specimens: pier column specimens without SSAWC or LCSS. G1 included a specimen strengthened with AWC and LCSS. G2 included five specimens strengthened using the IPCSAM; G2 samples were used to explore the effects of different control variables on the seismic performance of the strengthened piers. Five comparison groups were set up as follows: (a) Comparisons between UP-1 and RP-1, UP-2 and RP-4, and UP-3 and RP-5 to investigate the seismic strengthening effect of the piers strengthened using the IPCSAM under the same length–diameter ratio; (b) Comparison between RP-0 and RP-1 to investigate the effect of the self-stress produced using SSAWC on the seismic performance of strengthened piers; (c) Comparison between RP-1 and RP-2 to investigate the effect of the reinforcement ratio of LCSS on the seismic performance of strengthened piers; (d) Comparison between RP-1 and RP-3 to investigate the effect of the initial damage on the seismic performance of strengthened piers and verify the repair effect of the IPCSAM technology on the initial pier damage; (e) Comparison between RP-1, RP-4, and RP-5 to investigate the effect of the length–diameter ratio of the LCSS on the seismic performance of strengthened piers. According to relevant research [25], the errors for three test specimens with the same parameters are generally within 10%. Hence, to accelerate the test process, the preparation of only one specimen with the same parameters as in this experiment was sufficient. The values of the control variables were determined using Reference [2] and Code [55,56].

2.1.2. Unreinforced Core Pier Column Design

Considering the difficulty in specimen preparation and the inaccuracy caused by the size effect, 1/5 model proportions were adopted according to relevant studies [2,18]. The dimensions of the unreinforced core pier columns were as follows: diameter, 250 mm; heights, 1, 1.5, and 2 m. A bearing platform with dimensions of 500 mm (length) × 500 mm (width) × 400 mm (height) was set at the top of the pier column to apply cyclic horizontal loading. Another bearing platform with dimensions of 1000 mm (length) × 700 mm (width) × 500 mm (height) was set at the bottom of the pier column to fix the specimen tightly to the ground. The concrete strength grade for the unreinforced core pier columns was C30 (concrete with a nominal compressive strength of 30 MPa), the concrete cover depth was 20 mm, the reinforcement ratio was 0.96%, and the axial compression ratio was 0.2. Other material properties of the concrete and steel bars in the unreinforced core pier columns

are listed in Tables 2 and 3. The detailed dimensions and reinforcement layouts of the pier columns are presented in Figure 2: *a* and *b* represent the height of the column body and the total height of the specimen, respectively. HRB400 grade was used for the longitudinal reinforcements with a 10 mm diameter. HPB300 grade stirrups with 6 and 8 mm diameters were used. The stirrup spacing in the densification area scope was 40 mm. The densification area scope of the specimen stirrups with diameters of 1, 1.5, and 2 m were 280, 400, and 480 mm in length, respectively.

Table 1. Main design parameters and grouping of the specimens.

Group	Specimen	Core Pier Column			SSAWC			LCSS	
		D × H (mm)	LDR	Initial Damage	Thickness (mm)	Self-Stress (MPa)	Reinforcement Ratio (%)	Thickness (mm)	Reinforcement Ratio (%)
G0	UP-1	250 × 1000	4	Intact					
	UP-2	250 × 1500	6	Intact					
	UP-3	250 × 2000	8	Intact					
G1	RP-0	250 × 1000	4	Intact	40	0	0.28	40	0.5
G2	RP-1	250 × 1000	4	Intact	40	1.6	0.28	40	0.5
	RP-2	250 × 1000	4	Intact	40	1.6	0.28	40	0.25
	RP-3	250 × 1000	4	Damaged	40	1.6	0.28	40	0.5
	RP-4	250 × 1500	6	Intact	40	1.6	0.28	40	0.5
	RP-5	250 × 2000	8	Intact	40	1.6	0.28	40	0.5

Note: (a) UP and RP represent the unreinforced and reinforced specimens, respectively. (b) D, H, and LDR represent the diameter, height, and length-diameter ratio, respectively, of the unreinforced core pier column. (c) The reinforcement ratio of the LCSS can be weakened by reducing the number of welded steel wire mesh layers in the segment. Reinforcement ratios of 0.25% and 0.5% represent the setting of one and two layers of wire mesh in the segment sleeve, respectively.

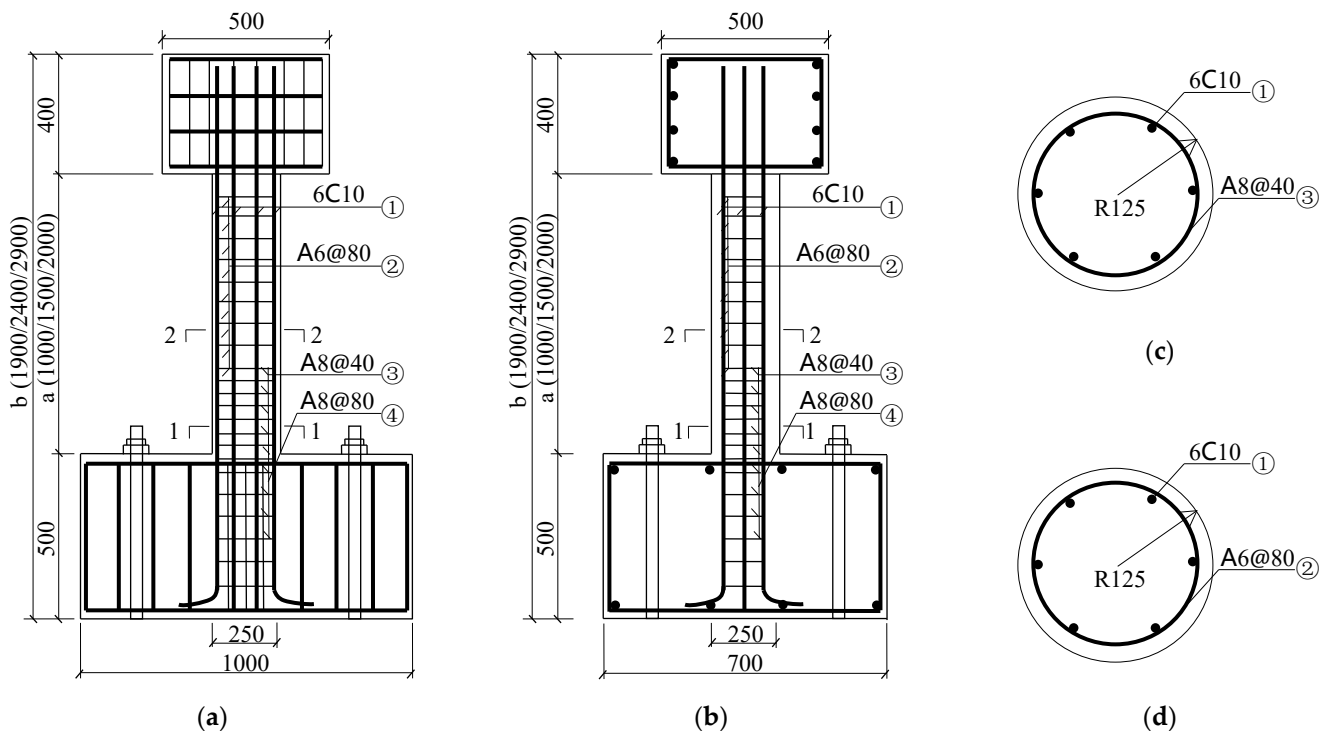


Figure 2. Dimensions and reinforcement layout of the core pier columns (unit: mm). (a) Front view; (b) Side view; (c) 1–1 profile; (d) 2–2 profile.

2.1.3. LCSS Design

Based on previous research results [2], the LCSS design included structural and connection components. For the structural design, the pre-assembly form and segment dimensions were determined. The sleeve ring comprised three standard segments, one adjusting segment, and a setting rabbet between them. To improve the strength and durability of the LCSS as the structural reinforcement for the concrete segment, we set the double-layer

welded steel wire mesh with a 1.2 mm diameter and mesh size of 25 mm × 25 mm in the segment [2]; the concrete strength grade was C40. The lengths of the upper and lower meshes in the standard segments were 375 and 320 mm, respectively. The lengths of the upper and lower meshes in the adjusted segments were 125 and 106 mm, respectively. The width of the wire mesh was 170 mm. The segments' inner and outer diameters, thickness, and height were 165, 205, 40, and 170 mm, respectively. Figure 3 shows the structure of the LCSS.

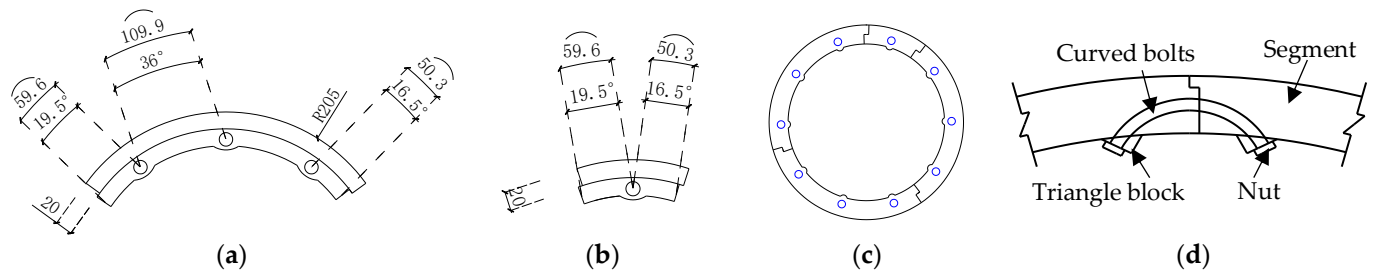


Figure 3. Structure and connection of the LCSS. (a) Standard segment; (b) Adjusting segment; (c) Segment ring; (d) Circumferential connection.

For the connection design, the holes were reserved using pre-embedded PVC pipes to fix the bolts, and curved bolts and triangular blocks were used for the circumferential connection of the segments. Long bolts and nuts were used for the longitudinal connection of the segments by reserving the holes. The diameters of the PVC pipes, circumferential bolts, and longitudinal bolts were 16, 6, and 8 mm, respectively. Three circumferential connections were equally spaced longitudinally around each ring segment, and 10 longitudinal connections were arranged at equal intervals along the circumference. The connections between the segments are shown in Figure 3, while the LCSS and prefabricated molds are shown in Figure 4. The material properties of the concrete, welded steel wire mesh, and bolts in the LCSS are presented in Table 3.

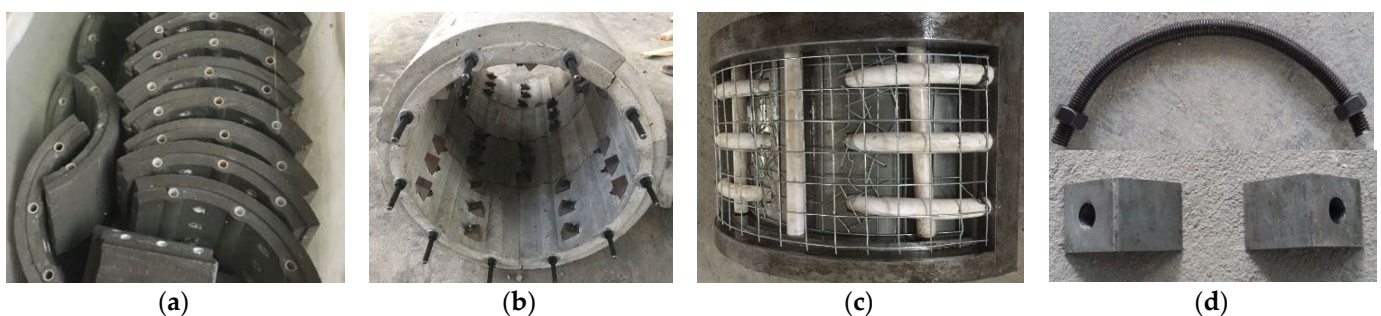


Figure 4. LCSS and prefabricated mold. (a) Segments; (b) Sleeve; (c) Prefabricated mold of segments; (d) Curved bolts and triangle blocks.

2.1.4. SSAWC Design

As the filling material connecting the core pier column and LCSS, the SSAWC directly affects the seismic performance of the strengthened specimens. Wu and Jiang [1] proposed the optimal mixture ratio for C40 SSAWC using the orthogonal test design and range analysis. The materials and mixture ratios of the AWC were the same as those of the SSAWC, although the expansive agent was equivalently replaced by cement. The mixture ratios and properties of the filled concrete were adjusted according to the Chinese codes [57–60] and are presented in Tables 2 and 3, respectively. The thickness of the filled concrete was 40 mm, according to a previous study [2]. A steel wire mesh with a diameter of 1.2 mm and mesh size of 25 mm × 25 mm was used as the internal reinforcement of the filled concrete, and the constructional reinforcement ratio was set to 0.28%. Referring to

previously reported formulas for calculating the self-stress value of concrete-filled steel tubes [61], the self-stress value of the SSAWC was calculated as 1.6 MPa.

Table 2. Mixture ratio of the filled concrete (unit: kg/m³).

Filled Concrete	Cement	Expansive Agent	Anti-Dispersion Agent	Sand	Stone	Water-Reducing Agent	Water
SSAWC	460.98	51.22	15.37	623.28	923.92	7.68	210
AWC	512.20	0	15.37	623.28	923.92	7.68	210

Table 3. Material properties of the specimens.

Material	Elastic Modulus (GPa)	Compressive Strength (MPa)	Axial Compressive Strength (MPa)	Axial Tensile/Yield Strength (MPa)	Poisson's Ratio	Area (mm ²)	Initial Setting Time (h)	Final Setting Time (h)
C30 concrete in column	29.61	29.51	22.43	2.54	0.2		11.6	16.2
C40 filled concrete (AWC)	33.16	42.56	32.35	3.11	0.2		18.3	21.0
C40 filled concrete (SSAWC)	33.23	42.88	32.59	3.12	0.2		15.4	17.8
C40 concrete in LCSS	33.45	43.96	33.72	3.16	0.2		9.5	14.4
Welded steel wire mesh	180			210	0.3	1.13		
10 mm HRB400 steel rebar	200			415	0.3	78.50		
8 mm HPB300 steel rebar	200			355	0.3	50.24		
6 mm HPB300 steel rebar	200			351	0.3	28.26		
Circumferential/longitudinal bolts	206			640	0.3	28.26/50.24		

2.2. Specimen Preparation

(1) The production process for the unreinforced specimens is shown in Figure 5: (a) the reinforcement cage was assembled; (b) formwork support was conducted; and (c) concrete was poured and cured. The initial damage to specimen RP-3 was inflicted by weakening a certain volume of the column body concrete before reinforcement. The position and volume of the weakened portion were calculated using finite element software ABAQUS 6.13. Foam, comprising 30% of the column's cross-sectional area with a 40 mm height, was used to fill the calculated weakened section 30 cm from the top surface of the bottom-bearing platform when concrete was poured. The core pier column of RP-3 with initial damage was obtained by dissolving the foam in xylene after formwork removal (Figure 5d).

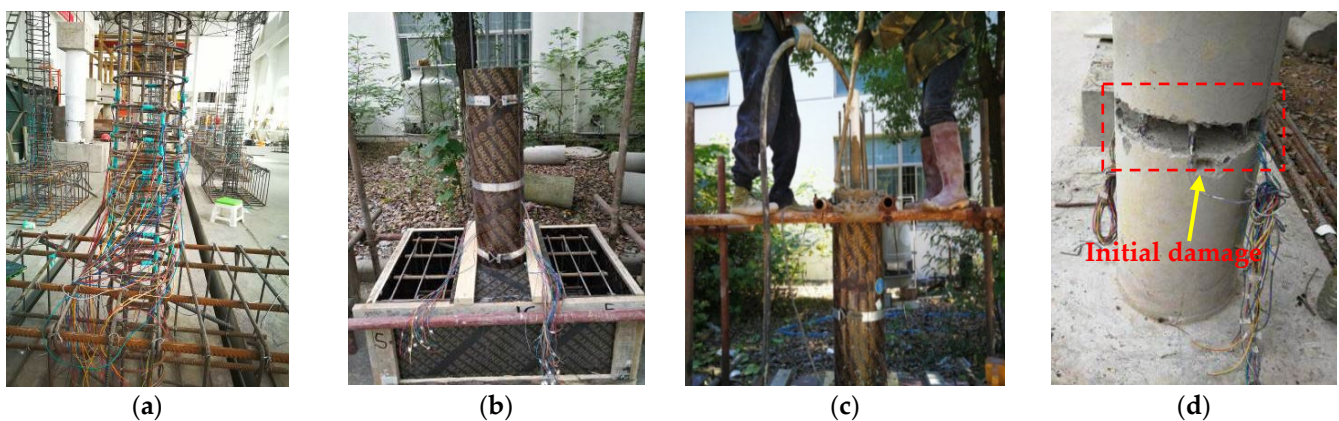


Figure 5. Production process for the unreinforced specimens. (a) Assembling reinforcement cage; (b) Formwork support; (c) Pouring concrete; (d) Creating the initial damage.

(2) For the strengthened specimens, a steel bucket with a 600 mm diameter and 950 mm height was filled with water and used to simulate the underwater environment. The production process is shown in Figure 6: (a) the unreinforced core pier column was placed after artificial chiseling in the bucket; (b) the assembled LCSS and welded steel wire

mesh were laid in sequence; (c) the bucket was filled with water, and the SSAWC was poured and cured.

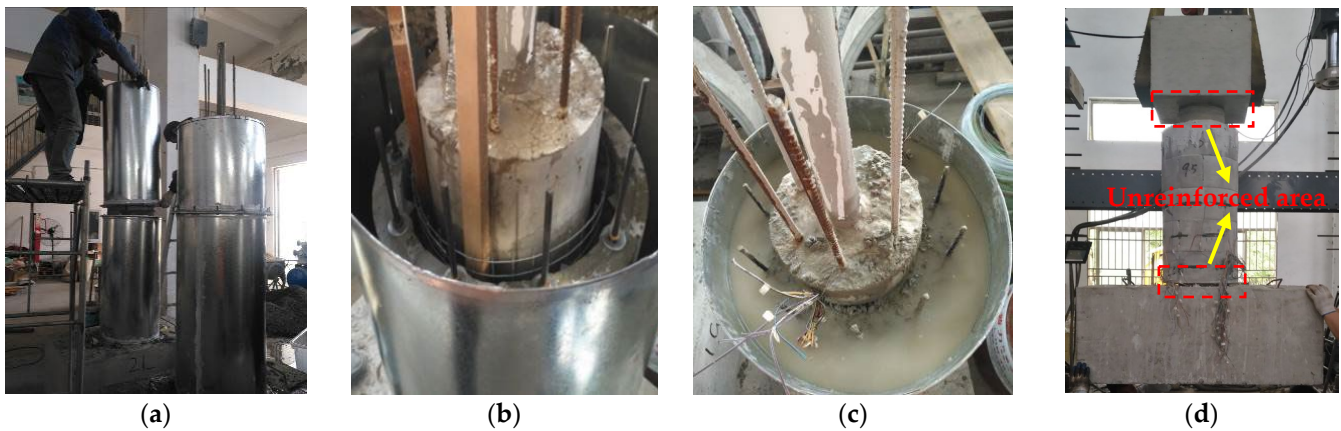


Figure 6. Production process for the strengthened specimens. (a) Installing steel sleeve and injecting water; (b) Laying LCSS and welded steel wire mesh; (c) Pouring SSAWC and performing concrete curing; (d) Unreinforced areas of the specimens.

Considering the limitations of the prefabricated mold used for the segments, the LCSS was impossible to scale in equal proportions, resulting in a relatively thick LCSS. When the pier column reaches a certain lateral displacement, the full-length LCSS experiences non-predictive local compression damage due to the first contact with the bearing platform at the top or bottom of the pier column, which further influences the seismic strengthening effect and accuracy of the test results. Therefore, to avoid this phenomenon in the quasi-static test, we reserved 30 cm and 20 mm areas without strengthening at the top and bottom of the specimens, respectively (Figure 6d). The stirrups in the unreinforced area at the bottom of the pier column were densified (Figure 2).

2.3. Test Setup

Each specimen was first anchored to a strong floor and reaction wall using prestressed steel bolts to prevent sliding during the test. Details of the loading setup are shown in Figure 7. All specimens were tested under a combination of constant axial and lateral cyclic loads. During the test, a constant target axial load corresponding to an axial compression ratio of 20% was first applied to the top of the specimen using a 30-t hydraulic jack through three steel strands passing through the pre-buried bellows at the center of the pier column. Consequently, the load was transferred to the specimen evenly and stably. A lateral cyclic load was then applied to the side of the top-bearing platform using a 50-t electrohydraulic servo horizontal actuator, and the displacement loading rate was set to 0.1 mm/s. The protocol for the cyclic displacement–control load is shown in Figure 8 and was obtained according to the “Specification for seismic test of buildings” code [62–65]. Additionally, Δ_y was defined as the yield displacement of a test specimen. One cycle was imposed with 2 mm increments for each loading step. After the specimen entered the yield stage, the lateral load repeated three cycles at the displacement levels of $1\Delta_y$, $2\Delta_y$, $3\Delta_y$, . . . , and the test was terminated once the lateral bearing capacity of the specimen decreased to 85% of the peak load or the specimen exhibited severe damage. The lateral load and displacement were recorded using a horizontal actuator. Two linear variable displacement transducers (LVDTs) were used to measure the lateral displacements at the top and bottom of the pier column. Several strain gauges were applied to record the strain in the longitudinal rebars and stirrups in the potential plastic hinge area of the pier column. The detailed configuration of the displacement meters and strain gauges is presented in Figure 9.

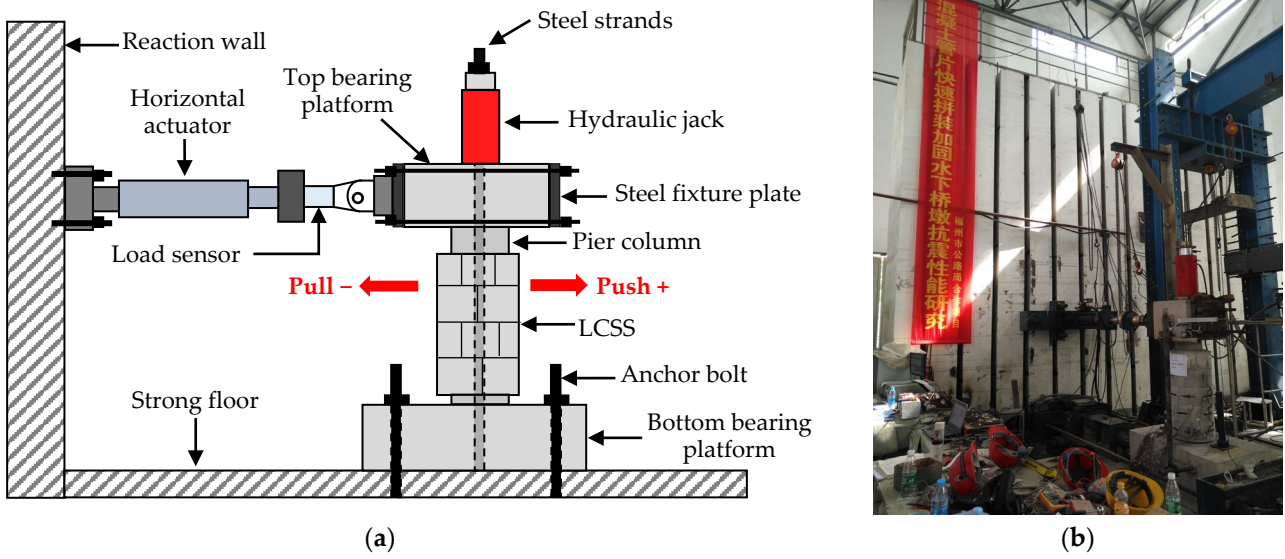


Figure 7. Layout of the experiment. (a) Loading system; (b) On-site photographs.

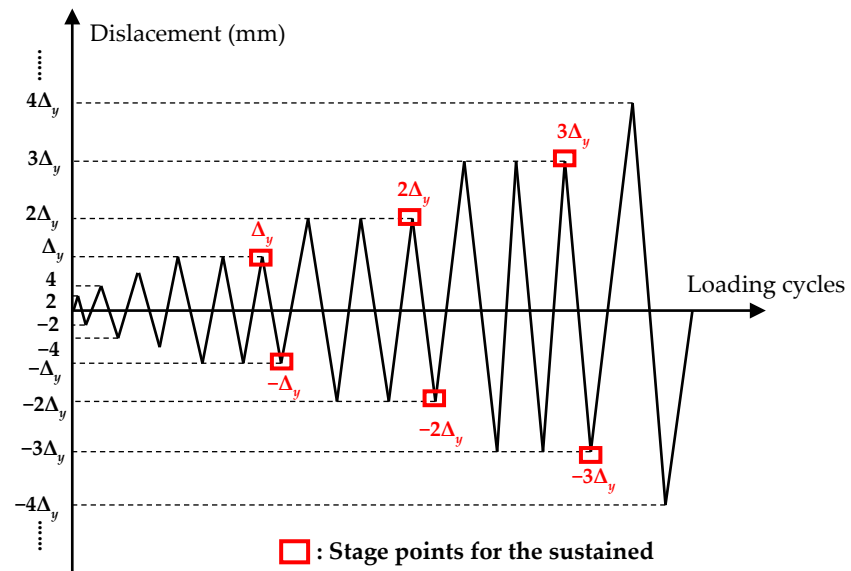


Figure 8. Protocol of the cyclic displacement-control load.

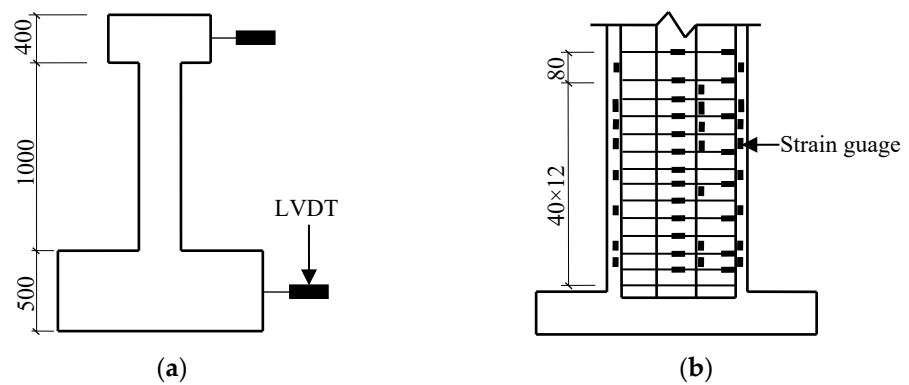


Figure 9. Layout of LVDTs and strain gauges. (a) LVDT distribution on pier columns; (b) Strain gauge distribution on steel rebars.

3. Experiment Results and Discussion

3.1. Failure Process and Modes

3.1.1. Unreinforced Specimens

As shown in Figure 10, all unreinforced specimens UP-1, UP-2, and UP-3 with different length–diameter ratios (4, 6, and 8) displayed flexural failure modes involving the crushing of concrete at the bottom of the pier column and buckling of longitudinal rebars. All unreinforced specimens experienced the generation, development, and expansion of bending and shear cracks, as well as the crushing of concrete at the pier column root. (a) For specimen UP-1, some initial circumferential fine transverse cracks appeared along the pier column bottom when the lateral displacement reached 6 mm. The longitudinal rebars yielded when the displacement reached 8 mm. It was generally considered that the specimen yielded due to the unrecoverable plastic deformation according to the hysteretic curve, and Δ_y was taken as 8 mm. At the end of the Δ_y displacement cycle, several transverse cracks began to expand approximately 15 mm from the pier column bottom. With the increase in load displacement, the original cracks continued to extend in the horizontal direction, and several new transverse cracks were generated on the surface of the pier column during the $2\Delta_y$ to $4\Delta_y$ loading cycles. During the $5\Delta_y$ loading cycles, some transverse cracks gradually developed into diagonal cracks and penetrated each other. Once the loading displacement reached $6\Delta_y$, the width of the penetrating cracks increased sharply, and slight spalling of concrete occurred around the cracks accompanied by a slight “splitting” sound. With further load displacement, the concrete on both sides of the tension and compression zone at the pier column bottom spalled off rapidly in blocks, and a plastic hinge gradually formed. Once the loading displacement increased to $8\Delta_y$, the concrete at the pier column root was crushed and exhibited significant peeling, leading to the longitudinal rebars and stirrups being exposed and buckling. Meanwhile, the horizontal load dropped to 85% of the peak load, and the test was terminated. (b) For specimen UP-2, when the lateral displacement reached 12 mm, several initial fine cracks began to appear at the pier column bottom; meanwhile, the longitudinal rebars had not reached the yield strength, and Δ_y was taken as 18 mm. During the $2\Delta_y$ to $6\Delta_y$ loading cycles, the transverse and diagonal cracks at the pier column bottom gradually widened, extended, and penetrated, resulting in concrete crushing and spalling at the column bottom and exposure of steel rebars at the pier column root. The test ended when the loading displacement reached $7\Delta_y$ due to the significant damage to the specimen. (c) For specimen UP-3, the initial cracks appeared when the lateral displacement reached 12 mm, and Δ_y was taken as 20 mm. During the $2\Delta_y$ to $9\Delta_y$ loading cycles, the development of cracks and damaged condition at the pier column root were similar to that of specimens UP-1 and UP-2. The test ended when the displacement reached $10\Delta_y$.

3.1.2. Strengthened Specimens

All strengthened specimens (RP-0 to RP-5) displayed flexural failure modes involving the crushing of concrete at the bottom of the core pier column and filling layer, as well as buckling and fracture of longitudinal rebars (Figure 11). All strengthened specimens experienced segment cracking, loosening of the circumferential connection of the segments, filled concrete crushing, concrete crushing and spalling at the core pier column root, longitudinal rebars pulling to fracture, and stirrups buckling. (a) In RP-1, the first transverse crack appeared at the pier column root when the lateral displacement reached 6 mm. Owing to the presence of LCSS, cracks on the surface of the core pier column could not be inspected during the test. The longitudinal rebar reached the yield strength when the displacement reached 8 mm, and the specimen reached yield strength, indicating that $\Delta_y = 8$ mm. During the Δ_y to $2\Delta_y$ loading cycles, several transverse cracks began to expand on the tensile side of the core pier column root. Subsequently, the initial transverse cracks widened and extended, gradually developing into diagonal cracks during the $3\Delta_y$ to $5\Delta_y$ loading cycles. Several new transverse cracks were also generated at the core pier column root. During the $6\Delta_y$ to $9\Delta_y$ loading cycles, the filled concrete and bottom concrete of the core pier column gradually

spalled due to the rapid development and penetration of cracks. Moreover, several vertical cracks appeared at the bottom of the LCSS, and part of the circumferential connection of the segments began to loosen and separate. Finally, during the $10\Delta_y$ to $11\Delta_y$ loading cycles, the concrete at the core pier column root was crushed, and vertical cracks at the LCSS developed rapidly. A “bang” was heard during this progress, which was considered to be due to a longitudinal rebar fracture. The test was terminated when the horizontal load decreased to 85% of the peak load. (b) The test failure processes of specimens RP-0, RP-2, and RP-3 were similar to those of RP-1. (c) The initial cracks for specimens RP-4 and RP-5 appeared at the core pier column root when the lateral displacement reached 12 mm, and Δ_y was set to 14 and 18 mm, respectively. Similar to that of RP-1, during the Δ_y to $8\Delta_y$ loading cycles for RP-4 and RP-5, cracks developed at the core pier column root and LCSS, the circumferential connection of the segments loosened, the bottom of the filled concrete was crushed, and crushing and spalling of the concrete occurred at the core pier column root.

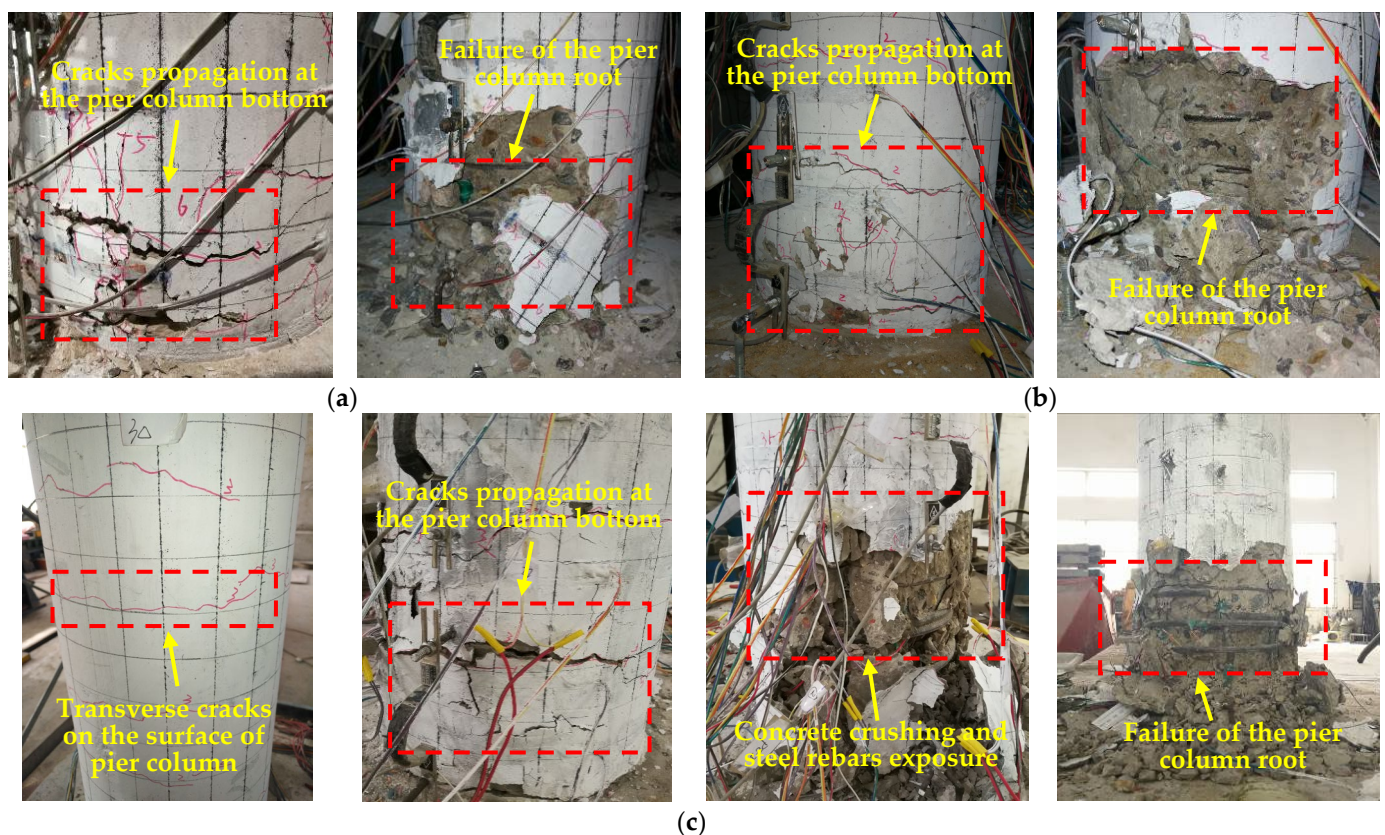


Figure 10. Typical failure phenomena and modes of unreinforced specimens. (a) UP-1; (b) UP-2; (c) UP-3.

Figure 11g,h shows the internal damage conditions at the bottom of the strengthened specimens via demolishing the segment sleeves and filled concrete in sequence after the test. Both the segment sleeves and filled concrete remained relatively intact, indicating that the LCSS and SSAWC designs could satisfy the seismic strengthening demand.

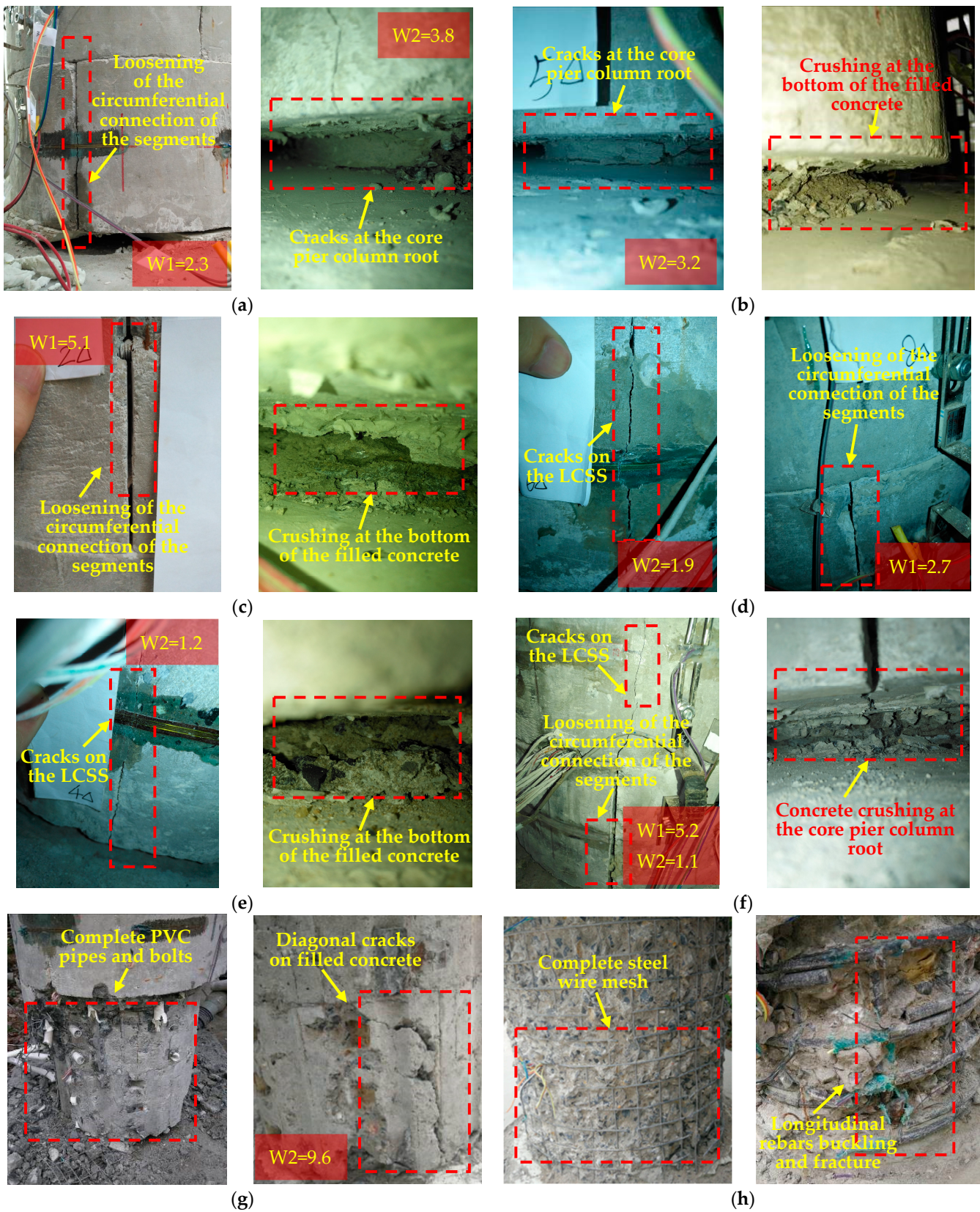


Figure 11. Typical failure phenomena and modes of strengthened specimens. (a) RP-0; (b) RP-1; (c) RP-2; (d) RP-3; (e) RP-4; (f) RP-5; (g) Demolition of the segment sleeves; (h) Demolition of the filled concrete. Note: W1 represents the average looseness width of LCSS, W2 represents the average crack width of concrete (unit: millimeters).

3.2. Seismic Performance Analysis

3.2.1. Experimental Results of Seismic Performance Indicators

(1) Hysteretic Curves and Skeleton Curves

The force–displacement hysteretic models of all specimens during the loading process are shown in Figure 12a–i. The hysteretic curves of all unreinforced specimens exhibited a “bow” shape with a noticeable pinching effect. Meanwhile, those of all strengthened specimens presented an “inverse S” shape, indicating that the bond-slip between steel bars and concrete existed in the loading process. Generally, for the strengthened specimens, at the initial loading stage, the lateral force was approximately proportional to the lateral displacement before the internal longitudinal rebars yielded, and the residual deformation, hysteresis loop area, and energy dissipation were small, reflecting the elastic state of the pier columns. With the increase in lateral displacement until reaching the peak point, the hysteresis loop became less steep, owing to the development of concrete cracks and slippage between the steel bars and concrete. The residual deformation and energy consumption increased step by step, and the stiffness gradually degraded, reflecting the elastic–plastic stage of the pier columns. After reaching the peak load, the energy-dissipation capacity of the specimens continued to improve; however, the bearing capacity and stiffness rapidly degraded until the specimens were damaged.

Comparisons of the skeleton curves of all specimens are shown in Figure 12j. (a) Those between reinforced specimens (i.e., RP-0 to RP-5) and unreinforced specimens (i.e., UP-1 to UP-3) indicate that the bearing capacity and initial stiffness of reinforced specimens were much higher than those of unreinforced specimens; however, the peak and ultimate displacement of reinforced specimens are generally lower than those of unreinforced specimens. The comparison between UP-1 and RP-1, UP-2 and RP-4, and UP-3 and RP-5 shows that IPCSAM can effectively improve the bearing capacity and initial stiffness of the pier column. (b) The comparison between RP-0 and RP-1 shows that SSAWC with a self-stress of 1.6 MPa can effectively improve the bearing capacity and initial stiffness of the pier column. (c) The comparison between RP-1 and RP-2 indicates that a 0.25% increase in the reinforcement ratio of LCSS can effectively improve the bearing capacity of the pier column. (d) The comparison between RP-1 and RP-3 shows that initial damage has a relatively small impact on the bearing capacity and initial stiffness of the pier column. (e) The comparison between RP-1, RP-4, and RP-5 indicates that the larger the length–diameter ratio of the reinforced specimen, the greater the bearing capacity and initial stiffness, and the smaller the peak and ultimate displacement.

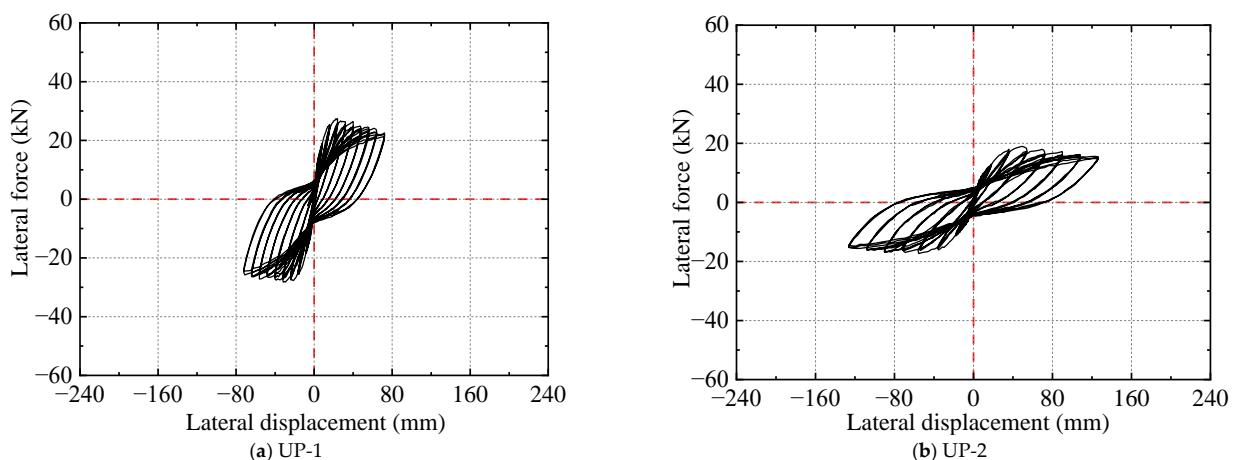


Figure 12. Cont.

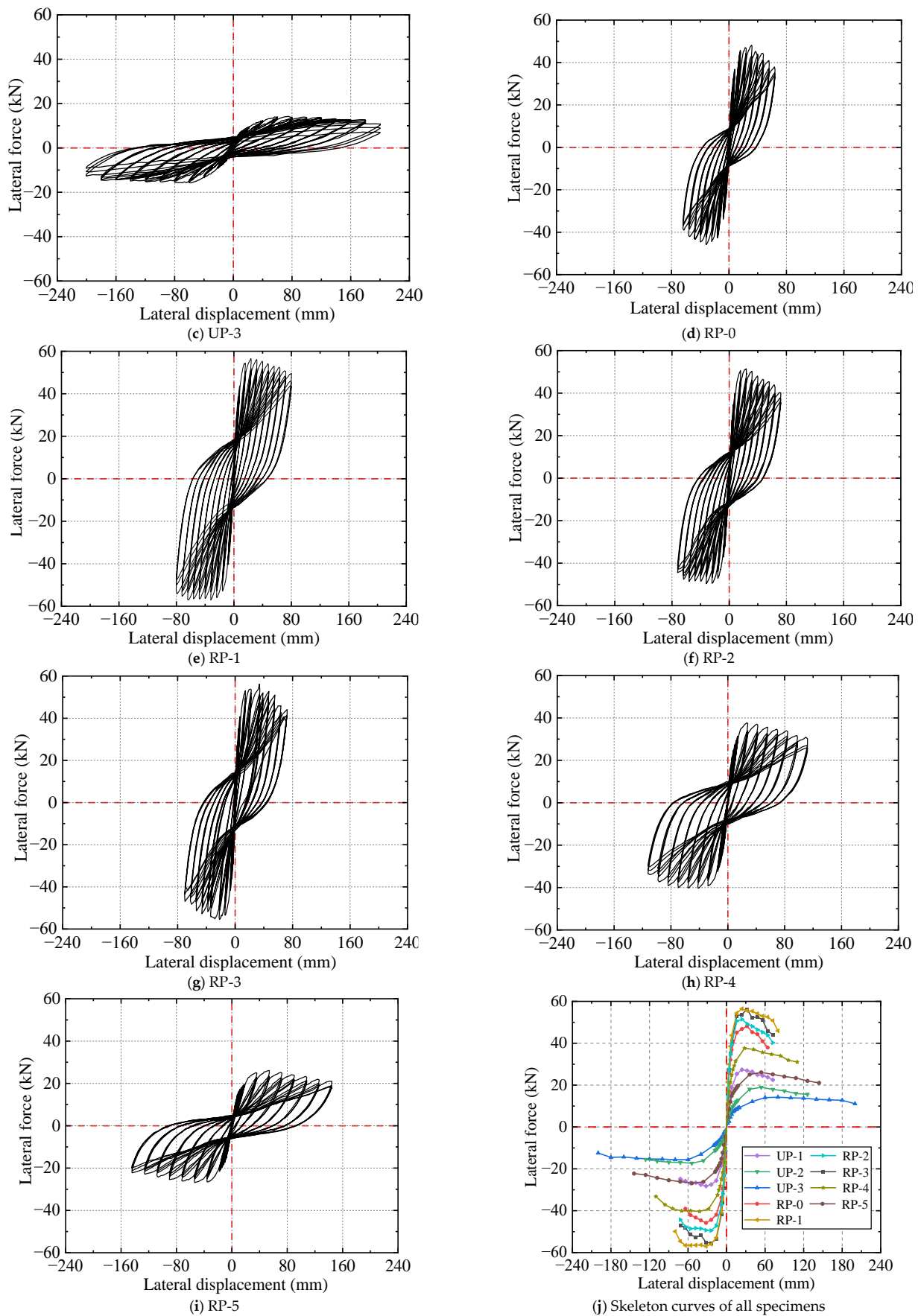


Figure 12. Hysteretic and skeleton curves of specimens (a–j).

(2) Bearing Capacity, Displacement, and Ductility

The bearing capacity, displacement, and ductility coefficients of all specimens at different loading stages, obtained from the skeleton curves in Figure 12, are listed in Table 4. To evaluate the ductility of the specimens, we defined the ratio of the ultimate displacement Δ_u to the yield displacement Δ_y as the ductility coefficient μ , calculated using Equation (1), as follows:

$$\mu = \frac{\Delta_u}{\Delta_y} \tag{1}$$

Table 4. Feature point values of specimen skeleton curves.

Specimen	K_0 (kN/mm)	F_y (kN)	Δ_y (mm)	F_p (kN)	Δ_p (mm)	F_u (kN)	Δ_u (mm)	μ
UP-1	4.53	22.07	11.93	27.37	23.85	23.26	67.22	5.63
UP-2	1.54	13.86	21.71	18.94	53.94	16.09	105.94	4.88
UP-3	0.88	11.63	36.33	14.22	78.73	12.08	186.74	5.14
RP-0	7.69	38.46	9.56	48.16	31.59	40.93	56.02	5.86
RP-1	8.33	45.25	9.11	56.48	23.53	48.01	76.58	8.41
RP-2	7.17	41.28	9.36	51.46	22.82	43.74	64.37	6.88
RP-3	7.95	44.91	10.73	56.19	31.46	47.76	61.04	5.69
RP-4	4.26	30.38	13.06	37.62	27.37	31.97	95.70	7.33
RP-5	2.44	20.48	20.67	26.09	53.66	22.18	123.61	5.98

Note: (a) F_y and Δ_y represent the lateral force and displacement of yield point, respectively. (b) F_p and Δ_p represent the lateral force and displacement of peak point, respectively. (c) F_u and Δ_u represent the lateral force and displacement of ultimate point, respectively. (d) K_0 refers to the initial stiffness, i.e., tangent stiffness at the origin. (e) μ refers to the ductility coefficient.

Owing to the lack of an evident yield point in the skeleton curves, a previously proposed farthest point method [66,67] was used to determine each specimen’s yield load and displacement. A schematic of the farthest point method is presented in Figure 13, which defines the yield point of the component as the point on the skeleton curve that is farthest from the line connecting the origin and peak point. The ultimate displacement Δ_u was defined as the displacement corresponding to the load decreasing to 85% of the peak load.

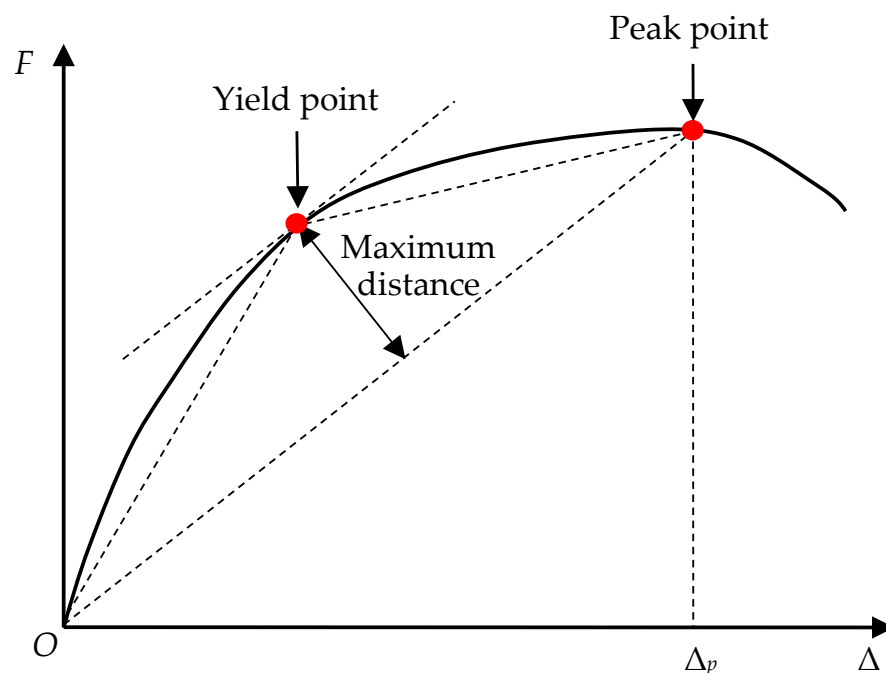


Figure 13. Farthest point method for determining the yield points of specimens.

(3) Stiffness degradation

The secant stiffness K_i was used to characterize the stiffness degradation of the specimens during the loading process, which was calculated using Equation (2):

$$K_i = \frac{|+F_i| + |-F_i|}{|+\Delta_i| + |-\Delta_i|} \tag{2}$$

where F_i represents the peak load of the first displacement cycle in the i -th loading step, and Δ_i represents the corresponding displacement of the F_i ; + and – represent the values obtained in the positive and negative directions, respectively.

The stiffness degradation curves of all testing specimens are shown in Figure 14; each specimen’s stiffness degradation curve was relatively symmetrical, with minor differences caused by construction deviation and material anisotropy [68]. The stiffness of all specimens decreased rapidly in the early stage with increased lateral displacement and then gradually flattened out.

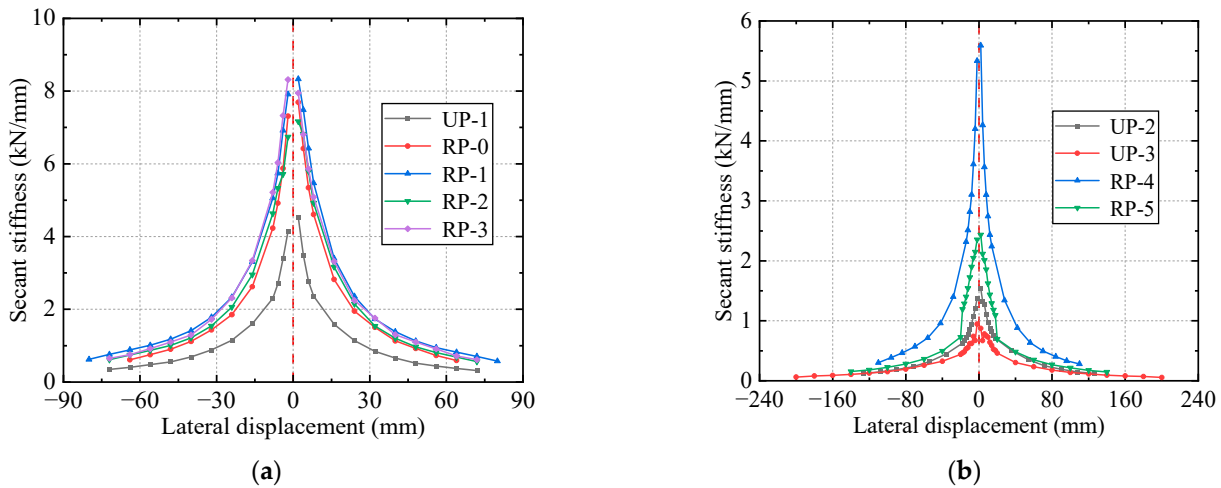


Figure 14. Stiffness degradation curves. (a) Secant stiffness of specimens with a length-diameter ratio of 4; (b) Secant stiffness of specimens with length-diameter ratios of 6 and 8.

(4) Energy Dissipation

According to the calculation proposed by Priestly [46] (Figure 15) and the code [62], the energy dissipation per cycle E_{hi} and the equivalent viscous damping ratio ζ_{eqi} were adopted to quantify the seismic energy absorption ability of specimens in the i -th loading step, calculated using Equations (3) and (4):

$$E_{hi} = S_{i(ABC+CDA)} \tag{3}$$

$$\zeta_{eqi} = \frac{1}{2\pi} \cdot \frac{S_{i(ABC+CDA)}}{S_{i(OBE+ODF)}} \tag{4}$$

where $S_{i(ABC+CDA)}$ represents the envelope area of the hysteretic loop in the i -th loading step, and $S_{i(OBE+ODF)}$ represents the sum of the areas of triangles OBE and ODF. The energy dissipation curves of all specimens are shown in Figure 16.

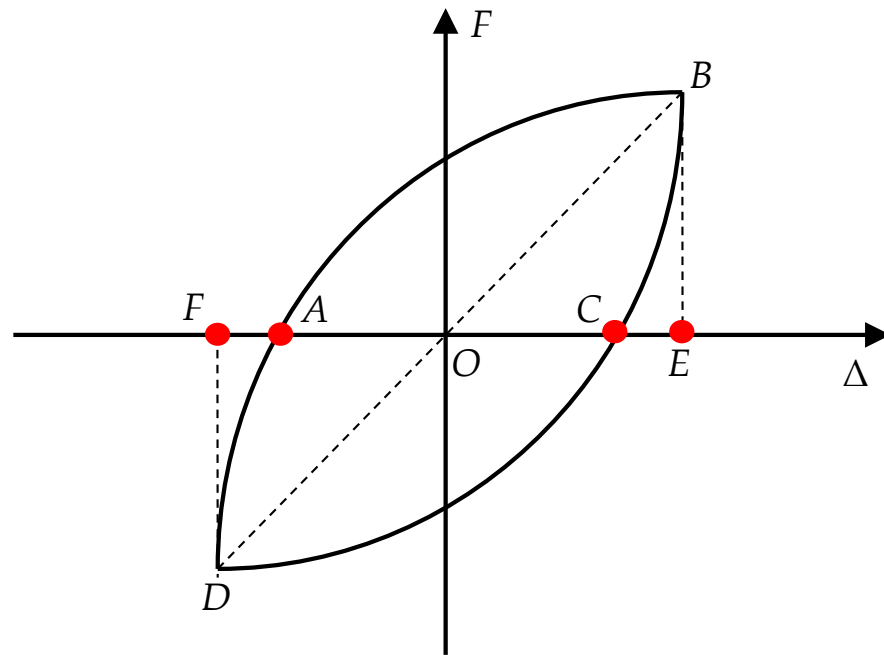


Figure 15. Calculation diagram for energy dissipation.

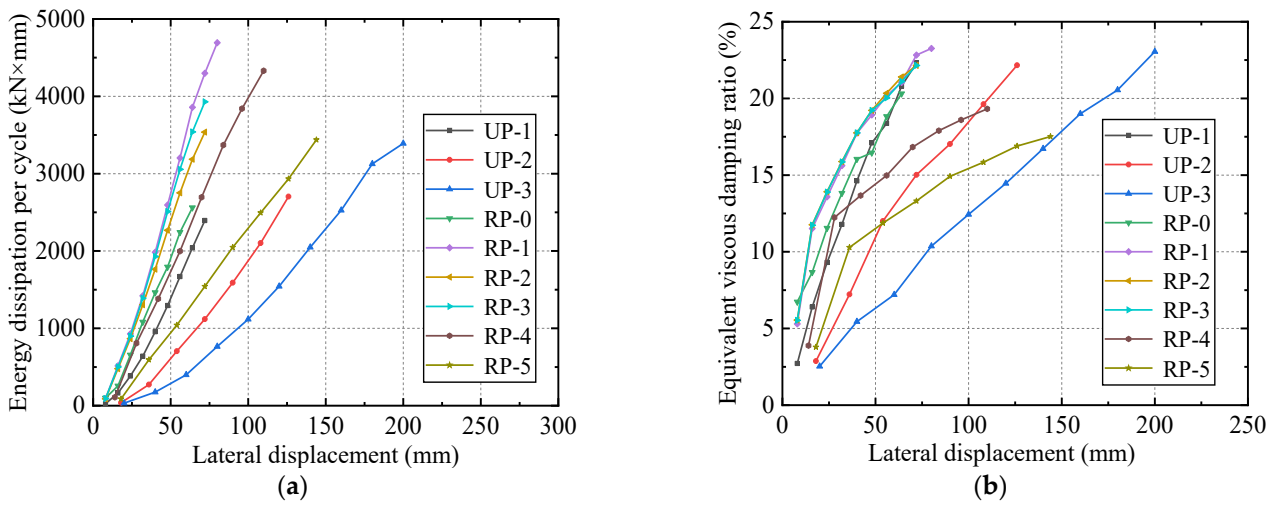


Figure 16. Energy dissipation curves. (a) Energy dissipation per cycle; (b) Equivalent viscous damping ratio.

3.2.2. Comparative Analysis Based on Different Influencing Factors

(1) Seismic strengthening effect of the IPCSAM

As shown in Table 4, the comparison between UP-1 and RP-1, UP-2 and RP-4, and UP-3 and RP-5 with the same length–diameter ratio (i.e., 4, 6, and 8, respectively) indicated that the peak load F_p of RP-1, RP-4, and RP-5, which were strengthened using the IPCSAM, increased by 106.4%, 98.6%, and 83.5%, respectively. The initial stiffness K_0 increased by 83.9%, 176.6%, and 177.3%, respectively, and the ductility coefficient μ increased by 49.4%, 50.2%, and 16.3%, respectively. In addition, the secant stiffness K_i , energy dissipation per cycle E_{hi} , and equivalent viscous damping ξ_{eqi} of RP-1, RP-4, and RP-5 at each loading stage were significantly higher than those of UP-1, UP-2, and UP-3 (Figures 14 and 16). Generally, the bearing capacity, ductility, stiffness, and energy dissipation capacity of the strengthened specimens were significantly improved compared with the unreinforced

specimens, indicating that the IPCSAM had a good seismic strengthening effect on pier columns with different length–diameter ratios.

(2) Influence of self-stress on the strengthening effect

As shown in Table 4, the comparison between specimens RP-0 and RP-1 showed that an initial circumferential self-stress of 1.6 MPa increased the peak load F_p , initial stiffness K_0 , and ductility coefficient μ of the strengthened specimen by 17.3%, 8.3%, and 43.5%, respectively. Meanwhile, compared with RP-0, the secant stiffness K_i , energy dissipation per cycle E_{hi} , and equivalent viscous damping ζ_{eqi} of RP-1 improved to a certain extent, and the stiffness degradation rates of the two specimens were similar (Figures 14 and 16). We can conclude that the circumferential self-stress generated by the SSAWC provided active restraint to the core pier column, placing it in a triaxial compression state, which effectively delayed the internal cracking of the pier column and enhanced its bearing capacity, ductility, stiffness, and energy dissipation capacity. Thus, the self-stress produced by the SSAWC significantly improves the seismic performance of strengthened pier columns.

(3) Influence of the LCSS reinforcement ratio on the strengthening effect

A comparison between RP-1 and RP-2 indicated that, with an increase in the reinforcement ratio of the LCSS from 0.25% to 0.5%, the peak load F_p , initial stiffness K_0 , and ductility coefficient μ of the strengthened specimens increased by 9.76%, 16.18%, and 22.24%, respectively (Table 4). The secant stiffness K_i also increased slightly during the entire loading process, while the stiffness degradation rates of the two specimens remained relatively constant (Figure 14). We inferred that the increased reinforcement ratio of the LCSS enhanced its tensile strength and stiffness, improving its circumferential constraint effect on the core pier column and ultimately increasing the strengthened pier columns' bearing capacity, ductility, and stiffness. Additionally, the energy dissipation per cycle E_{hi} of RP-1 was larger than that of RP-2 during the loading process, and the equivalent viscous damping ζ_{eqi} of RP-1 was similar to that of RP-2 (Figure 16), indicating that the increased reinforcement ratio of the LCSS could improve the energy dissipation capacity of the strengthened pier columns to a certain extent. In summary, enhancing the reinforcement ratio of LCSS can effectively improve the seismic performance of strengthened pier columns.

(4) Influence of initial damage on the strengthening effect

A comparison of RP-1 with RP-3 (Table 4) showed that initial damage reduced the peak load F_p , initial stiffness K_0 , and ductility coefficient μ of the strengthened specimens by 0.5%, 4.6%, and 32.3%, respectively. We inferred that the initial damage led to a slight weakening of the bearing capacity and initial stiffness of the pier column. Moreover, the damage accumulation between the initial damaged area and its filled concrete interface during the loading process inevitably weakened the ductility performance of the pier column. In addition, the secant stiffness K_i , energy dissipation per cycle E_{hi} , equivalent viscous damping ζ_{eqi} , and stiffness degradation rate of the two specimens were highly similar during the entire loading stage (Figures 14 and 16). Hence, the stiffness, bearing capacity, and energy dissipation capacity of the strengthened specimen with initial damage could be restored to a near-undamaged state.

(5) Influence of length–diameter ratio on the strengthening effect

A comparison of RP-1, RP-4, and RP-5 (Table 4) showed that the peak load F_p , initial stiffness K_0 , and ductility coefficient μ decreased as the length–diameter ratio of the strengthened specimen increased from 4 to 6 to 8, with total decreases of 53.8%, 70.7%, and 28.9%, respectively. Similarly, the secant stiffness K_i , energy dissipation per cycle E_{hi} , and equivalent viscous damping ζ_{eqi} significantly decreased with increased length–diameter ratios of the strengthened specimen during the entire loading stage (Figures 14 and 16). The larger the length–diameter ratio, the longer the effective length of the column and the greater the bending moment effect caused by the horizontal earthquake action, resulting in an apparent decrease in the bearing capacity, stiffness, ductility, and energy dissipation capacity of the strengthened pier columns.

4. Extended Parameter Analysis

To investigate the effects of influencing factors that were not excluded from the quasi-static test and the corresponding changes on the seismic performance of the strengthened pier columns and provide the necessary empirical support to establish restoring force models, we adopted finite element numerical models for extended parameter analysis. First, a numerical model of the strengthened pier column was established using ABAQUS. Second, the accuracy and reliability of the numerical model were verified using the experimental data. Finally, the influencing parameters directly related to the establishment of the restoring force model of the strengthened pier column, including the LCSS thickness, reinforcement ratio, strength, SSAWC self-stress, and pier column axial compression ratio [69–71], were selected to perform the extended parameter analysis.

4.1. Finite Element Numerical Model

4.1.1. Material Constitutive Relationship and Parameter Setting

As listed in Table 3, the material parameters of the concrete, rebar, stirrups, bolts, and welded wire meshes were set according to the measured values. A solid element was used to simulate concrete. The plastic-damage model provided by ABAQUS was adopted as the constitutive relationship between the concrete materials of the core pier column, filling layer, and segment sleeve in the elastic–plastic stage (i.e., nonlinear behaviors) and the irreversible concrete damage, such as plastic deformation accumulation and stiffness degradation. The plastic behavior of concrete was primarily defined using five parameters: dilation angle ψ , flow potential deviation value ϵ , ratio of ultimate compressive strength of biaxial to uniaxial σ_{b0}/σ_{c0} , ratio of the second stress invariants on the meridian plane of tension and compression K_c , and viscosity coefficient ν ; each parameter was obtained with reference to a previous study [47] (Table 5). The stress–strain curve of concrete was determined according to the previously described code [48,56], and the damage factors of the plastic-damage model were calculated according to the energy equivalent principle proposed by Sidoroff [49,50]. The rebars, stirrups, bolts, and welded wire meshes were simulated using a wire element, and a double broken line was adopted as the constitutive relationship of the steel. Schematics of the stress–strain curves of concrete and steel bars are shown in Figure 17. The tensile and compressive stress–strain curves of concrete were plotted in the same coordinate system, however, different proportions were obtained. Additionally, $f_{c,r}$ and $\epsilon_{c,r}$ denote the representative values of the uniaxial compressive strength of the concrete and the corresponding peak compression strain, respectively; $f_{t,r}$ and $\epsilon_{t,r}$ denote the representative values of the uniaxial tensile strength of the concrete and the corresponding peak tensile strain, respectively; $\epsilon_{c,u}$ represents the ultimate compressive strength of concrete; $f_{y,r}$ and ϵ_y denote the representative value of the yield strength of the steel bar and corresponding yield strain, respectively; $f_{st,r}$ and ϵ_u denote the representative value of the ultimate strength of steel bar and corresponding peak strain, respectively.

Table 5. Parameters of the plastic-damage model.

ψ	ϵ	σ_{b0}/σ_{c0}	K_c	ν
30	0.1	1.16	0.6667	0.005

4.1.2. Numerical Model Establishment

Based on the aforementioned material constitutive relationship and parameter settings, the model components of the steel-reinforced cage and strengthened concrete pier column were established and assembled (Figure 18a,b). The model's boundary conditions were set as follows: (a) the connection between segments was simulated using a hard contact [25], indicating that the contact surface was only under compression. (b) The connections between the rebar and pier column concrete and the bolts and segment concrete were simulated using an embedded connection. (c) Based on the research by Zhou [72] and Zhao [25], the binding connection was used to simulate the connection between the filled

concrete and its adjacent members, and the “Coulomb friction model” was adopted to simulate shear transmission. (d) The top and bottom surfaces of the models were simplified and coupled into one point; constraints were set in each direction of the point obtained from the top and bottom couplings, except in the Z-direction of the top coupling point. The axial pressure on the pier column was applied primarily through the top coupling point. The initial self-stress produced by the SSAWC was simulated by applying circumferential compressive stress to the surface of the pier column and the inner side of the segment.

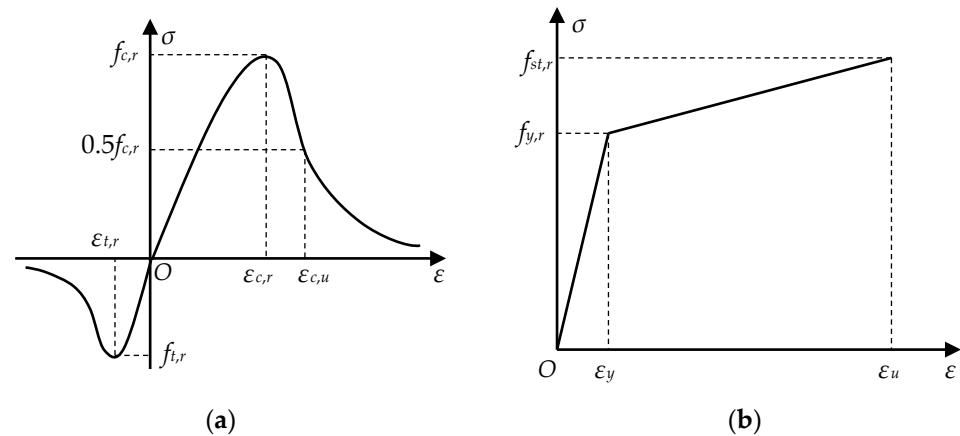


Figure 17. Constitutive relationship curves of concrete and steel bar. (a) Stress-strain curve of concrete; (b) Stress-strain curve of steel bar.

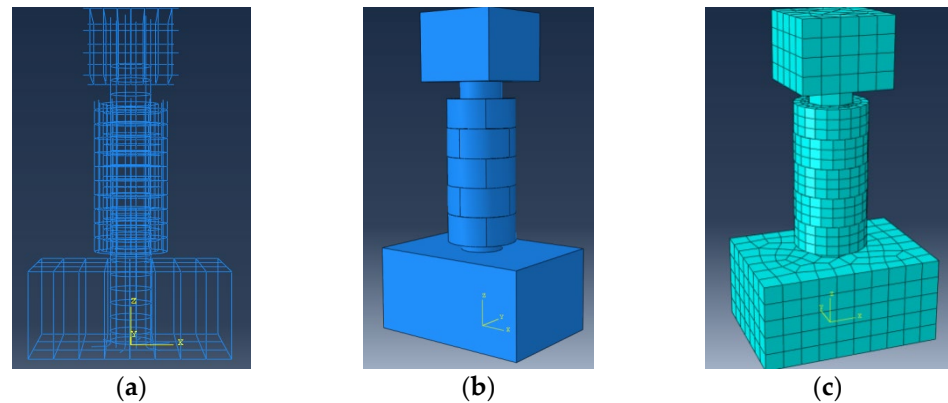


Figure 18. Finite element model. (a) Steel reinforced cage model after assembly; (b) Strengthened concrete pier column model after assembly; (c) Mesh division.

Regarding mesh division, when the grid spacing of the pier column body was <95 mm or the grid spacings of the filled concrete and segment sleeves were <65 mm, the finite element calculation results were difficult to converge, and the calculation cost was high. Thus, under the premise of comprehensive consideration of calculation accuracy and efficiency, the pier column body and filled concrete and segment sleeves adopted grid spacings of 100 mm and 70 mm, respectively (Figure 18c). Additionally, by calculating the finite element models with five different element sizes of the filled concrete and segment sleeves (i.e., 60 mm, 70 mm, 80 mm, 90 mm, and 100 mm), the maximum errors of the bearing capacity and ductility coefficient between different finite element models did not exceed 6% and 8%, respectively. Hence, the element size dependency of the finite element model was small and could be disregarded in this paper.

4.1.3. Numerical Model Verification

Two strengthened specimens, RP-0 and RP-1, were selected as the basic models to establish the corresponding numerical models, MRP-0 and MRP-1. The numerical sim-

ulation was performed according to the protocol of the cyclic displacement-control load shown in Figure 8. The accuracy and effectiveness of the finite element numerical model in Section 4.1.2 were verified by comparing the failure modes, skeleton curves, stiffness degradation curves, bearing capacity, and ductility between the test specimens and numerical models.

The stress cloud diagrams of the numerical models MRP-0 and MRP-1 after load failure were compared with the failure phenomena that appeared in the quasi-static test as follows (Figure 19). (a) The stress distribution of the steel rebars shows that the bottom longitudinal rebars and stirrups reached their ultimate stress when the pier column was damaged, consistent with the phenomenon in which the longitudinal rebars were pulled to fracture, and the stirrups buckled at the bottom of the strengthened specimens. (b) The stress distribution of the core pier column indicated that the concrete at the bottom reached the maximum compressive stress, corresponding with the crushing and spalling of the concrete at the bottom of the strengthened specimens. (c) Similarly, as indicated by the stress distribution of the filled concrete, the maximum stress at the bottom of the filled concrete during the failure of the pier column matched the occurrence of concrete cracking and spalling at the bottom of the filling layer of the strengthened specimens. (d) As observed in the stress distribution of the segment sleeve, the maximum stress of the segment ring concrete in the middle of the sleeve was consistent with the loosening of the circumferential connection and vertical cracking of the segments in the middle of the strengthened specimens.

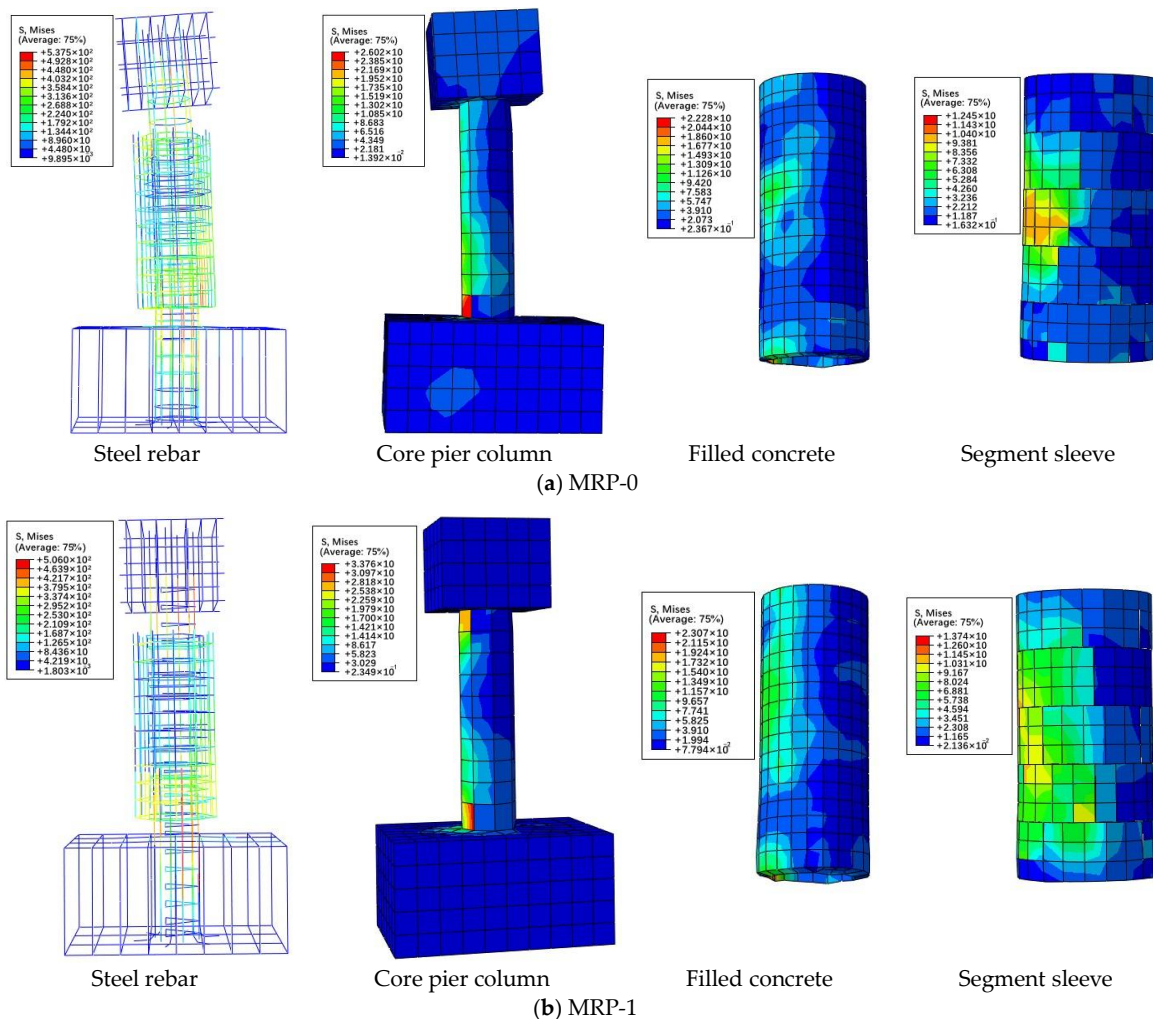


Figure 19. Stress cloud diagrams of numerical models after load failure (a,b).

As shown in Figures 20 and 21 and Table 6, (a) the skeleton curves of the numerical models were similar to those of the strengthened specimens. When the strengthened specimen reached the lateral bearing capacity, the downward trend of its skeleton curve was consistent with that of the numerical model, whereas the degradation rate of its bearing capacity was relatively high, and the maximum error between the skeleton curves was <15%. (b) The secant stiffness and stiffness degradation of strengthened specimens were relatively consistent with those of the numerical models, and the difference between the stiffness degradation curves was <10%. (c) The relative errors in the lateral bearing capacity and ductility coefficient between the strengthened specimens and numerical models were <5% and 10%, respectively, indicating that the specimens and models were in good agreement. Therefore, the numerical model corresponded well with the strengthened specimen, indicating that it can be used as a basic model for extended parameter analysis.

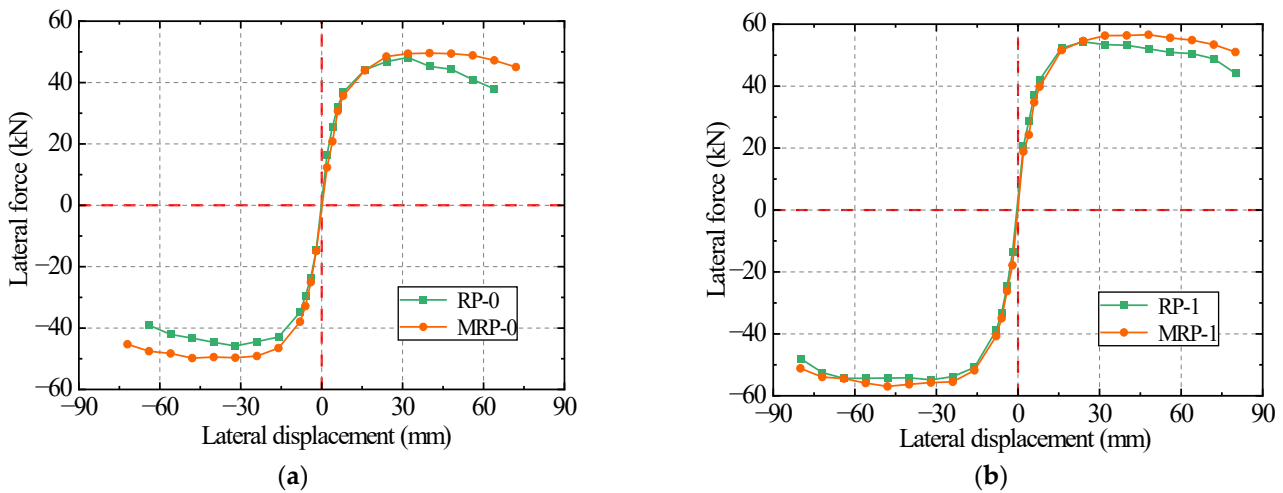


Figure 20. Comparison of skeleton curves between test specimens and numerical models. (a) Skeleton curves of RP-0 and MRP-0; (b) Skeleton curves of RP-1 and MRP-1.

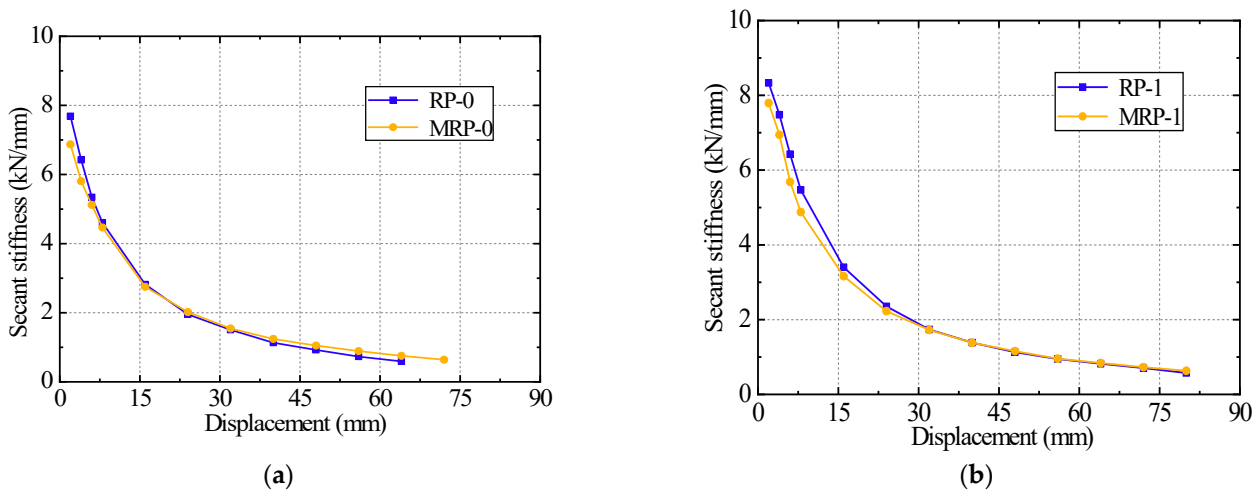


Figure 21. Comparison of stiffness degradation curves between test specimens and numerical models. (a) Secant stiffness of RP-0 and MRP-0; (b) Secant stiffness of RP-1 and MRP-1.

Table 6. Comparison of bearing capacity and ductility between test specimens and numerical models.

Specimen	F_p (kN)	RE of F_p (%)	Δ_y (mm)	Δ_u (mm)	μ	RE of μ (%)
RP-0	48.16	4.69	9.56	56.02	5.86	3.41
MRP-0	50.42		12.17	73.75	6.06	
RP-1	56.48	3.79	9.11	76.58	8.41	9.16
MRP-1	58.62		10.83	82.77	7.64	

Note: RE represents the relative error.

4.2. Results of Extended Parameter Analysis

The influencing parameters of the restoring force models for the strengthened specimens included the LCSS thickness, reinforcement ratio, strength, SSAWC self-stress, axial compression ratio, and length–diameter ratio of the pier column [48,49]. Considering that the influence of the length–diameter ratio on the hysteretic performance of the strengthened pier columns was studied in the quasi-static test, we established 20 numerical models based on the other five parameters for extended parameter analysis. We then investigated these five parameters' impact on the pier columns' seismic strengthening effect. Table 7 lists the main parameter settings for all numerical models. The other parameters, including the size, initial damage, and length–diameter ratio of the core pier column, filled concrete thickness, and segment sleeve reinforcement ratio, were set with reference to specimen RP-1 in Table 1. The material properties of the numerical models were set according to Table 3.

Table 7. Main parameter settings of all numerical models.

Model	Pier Column		SSAWC		LCSS
	ACR	Reinforcement Ratio (%)	Strength Grade	Self-Stress (MPa)	Thickness (mm)
MT-1	0.2	0.28	C40	1.6	20
MT-2	0.2	0.28	C40	1.6	30
MT-3	0.2	0.28	C40	1.6	40
MT-4	0.2	0.28	C40	1.6	50
MR-1	0.2	0.56	C40	1.6	40
MR-2	0.2	0.84	C40	1.6	40
MR-3	0.2	1.12	C40	1.6	40
MR-4	0.2	1.40	C40	1.6	40
MS-1	0.2	0.28	C30	1.6	40
MS-2	0.2	0.28	C35	1.6	40
MS-3	0.2	0.28	C40	1.6	40
MS-4	0.2	0.28	C45	1.6	40
MSS-1	0.2	0.28	C40	0	40
MSS-2	0.2	0.28	C40	1.6	40
MSS-3	0.2	0.28	C40	2.2	40
MSS-4	0.2	0.28	C40	2.8	40
MA-1	0.1	0.28	C40	1.6	40
MA-2	0.2	0.28	C40	1.6	40
MA-3	0.3	0.28	C40	1.6	40
MA-4	0.4	0.28	C40	1.6	40

Note: ACR represents the axial compression ratio of the pier column.

(1) Influence of LCSS thickness on the strengthening effect

As shown in Table 8 and Figure 22, as the segment thickness increased from 20 to 50 mm (i.e., the thickness–diameter ratio of the pier column increased from 1/20 to 1/8), the initial stiffness of the pier column increased by 33.18% owing to the increase in the column cross-section. Moreover, the peak load, ductility coefficient, and secant stiffness of the pier column first increased and then decreased. The ductility coefficient and peak load

reached their respective maximum values of 7.69 and 55.47 kN when the segment thickness was 30 and 40 mm, respectively. As the segment thickness increased from 40 to 50 mm, the peak load decreased gradually by 2.06%, whereas the ductility coefficient decreased rapidly by 11.38%. We inferred that an appropriate segment thickness could effectively improve the seismic performance indicators of the strengthened pier column. In contrast, an excessive segment thickness would cause intense sleeve stiffness, resulting in the core pier column and filling layer becoming the relatively seismically weak parts of the entire pier, failing before the sleeve, and weakening the bearing capacity and ductility of the pier column. Hence, the seismic strengthening effect is most advantageous for a pier column with a 400 mm diameter when the segment thickness is 40 mm (i.e., the thickness–diameter ratio is 1/10).

Table 8. Feature point values of all numerical models.

Model	K_0 (kN/mm)	F_y (kN)	Δ_y (mm)	F_p (kN)	Δ_p (mm)	F_u (kN)	Δ_u (mm)	μ
MT-1	15.07	32.05	10.91	45.36	56	42.87	80	7.33
MT-2	17.05	36.04	10.40	50.44	56	45.96	80	7.69
MT-3	17.98	43.70	11.24	55.47	48	50.48	80	7.12
MT-4	20.07	41.32	12.68	54.33	48	48.82	80	6.31
MR-1	15.47	40.53	11.32	49.77	40	46.33	80	7.07
MR-2	15.96	42.82	12.14	51.35	40	48.95	80	6.59
MR-3	17.86	43.68	13.49	54.03	48	50.19	80	5.93
MR-4	18.02	44.65	14.16	55.27	56	52.14	80	5.65
MS-1	14.73	34.13	10.99	47.33	56	43.02	80	7.28
MS-2	16.77	38.09	11.10	52.15	48	47.04	80	7.21
MS-3	17.98	44.05	11.48	55.47	48	50.48	80	6.97
MS-4	18.43	42.37	11.51	57.31	48	51.69	80	6.95
MSS-1	15.00	39.84	14.63	49.37	40	46.72	80	5.47
MSS-2	17.98	44.90	12.07	55.47	48	50.48	80	6.63
MSS-3	18.59	47.29	11.40	62.44	56	55.97	80	7.02
MSS-4	20.17	51.36	11.22	68.11	32	55.12	80	7.13
MA-1	13.35	38.22	11.17	48.62	40	44.14	80	7.16
MA-2	17.30	41.74	11.03	53.11	40	48.56	80	7.25
MA-3	17.98	44.78	11.99	55.47	48	50.48	80	6.67
MA-4	15.76	48.69	14.18	57.37	40	50.13	80	5.64

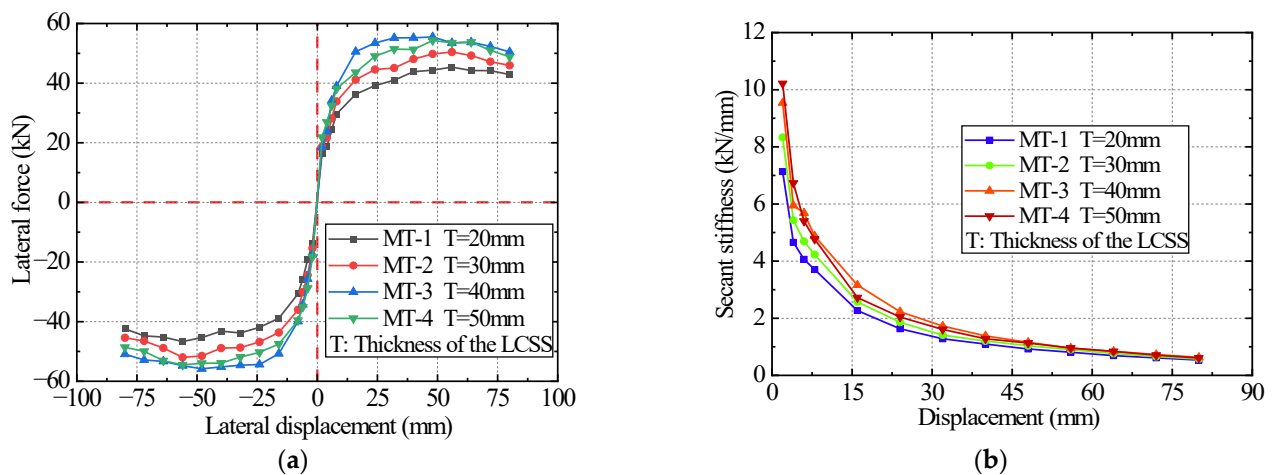


Figure 22. Comparison of the skeleton and stiffness degradation curves for numerical models with different LCSS thicknesses. (a) Skeleton curves of MT-1 to MT-4; (b) Stiffness degradation curves of MT-1 to MT-4.

(2) Influence of the SSAWC reinforcement ratio on the strengthening effect

Table 8 shows that the initial stiffness and peak load of the pier column increased by 16.48% and 11.05%, respectively, as the reinforcement ratio of the filled concrete increased from 0.56% to 1.40%. The secant stiffness increased to a certain extent, and the stiffness degradation rates of all models were relatively similar (Figure 23). Hence, we concluded that an appropriate increase in the filled concrete's reinforcement ratio could enhance the core column's stiffness and hoop constraint, improving the pier column's overall stiffness and bearing capacity. Meanwhile, the ductility coefficient continuously decreased with an increase in the reinforcement ratio, generally decreasing by 20.08%, indicating that the decrease in the ductility of the pier column was much higher than the increase in the bearing capacity and stiffness. This might have been due to the high reinforcement ratio causing the filled concrete to crush before the internal steel wire meshes yielded, resulting in reduced pier column ductility. Moreover, while the reinforcement ratio of the filled concrete increased, the increases in the peak and ultimate loads of the pier column were relatively small and maintained at approximately 2–5%, as calculated from Table 8. Hence, under the premise of meeting the design requirements of the bearing capacity of strengthened pier columns, it is desirable to use the smallest possible reinforcement ratio of filled concrete to maintain good ductility, such as adopting the constructional reinforcement ratio.

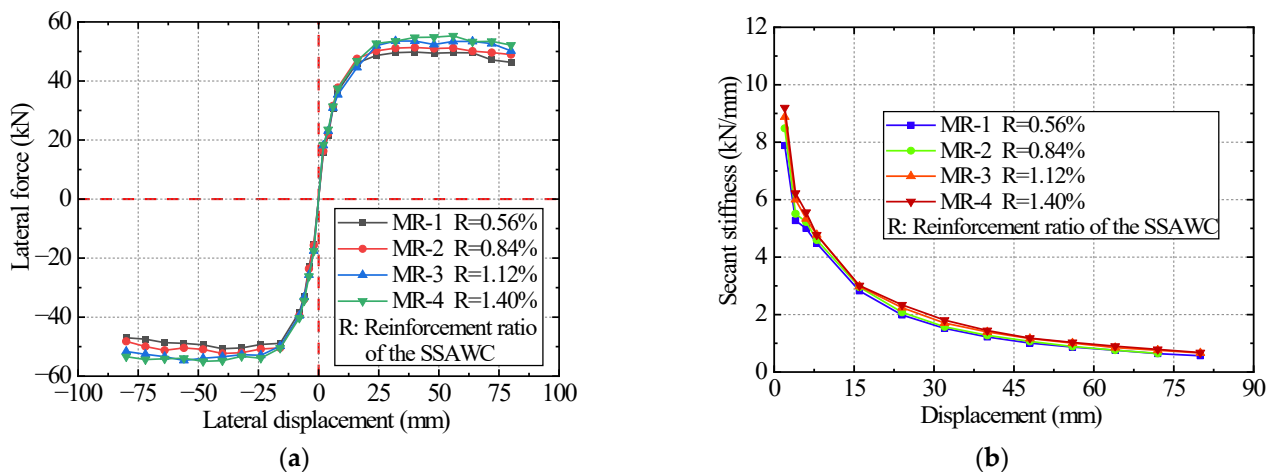


Figure 23. Comparison of the skeleton and stiffness degradation curves for numerical models with different SSAWC reinforcement ratios. (a) Skeleton curves of MR-1 to MR-4; (b) Stiffness degradation curves of MR-1 to MR-4.

(3) Influence of SSAWC strength on the strengthening effect

As shown in Table 8, with an increase in the strength grade of the filled concrete from C30 to C45, the initial stiffness and peak load of the pier column increased by 25.12% and 21.09%, respectively; however, the ductility coefficient generally decreased by 4.53%. When the concrete strength increased by one grade, the peak load increased by approximately 2–5 kN, and the ductility coefficient decreased by approximately 0.02–0.25. An appropriate increase in the filled concrete strength effectively enhanced the stiffness of the filling layer and the hoop constraint of the core column, further improving the strengthened pier column's overall stiffness and bearing capacity. However, with an increase in the filled concrete strength grade, the growth rate of the peak load decreased from 10.18% to 6.37% to 3.32%, and the growth rate of the ultimate load decreased from 9.34% to 7.31% to 2.40%, as calculated from Table 8. The ductility coefficient decreased during this process, indicating that the excessive strength grade (i.e., >C40) of the filled concrete provided limited improvement in the seismic performance of the pier columns and could lead to rapid ductility degradation. Moreover, the secant stiffness and stiffness degradation trends of MS-2, MS-3, and MS-4 were relatively the same and significantly higher than those of MS-1 (Figure 24). Hence, the high strength of the filled concrete could not significantly improve the secant stiffness. In summary, setting the filled concrete strength of the strengthened pier

column to be 1–2 grades higher than the concrete strength of the core column is sufficient. That is, the filled concrete strength grade should not exceed C40 for strengthened piers with a core column of C30 concrete.

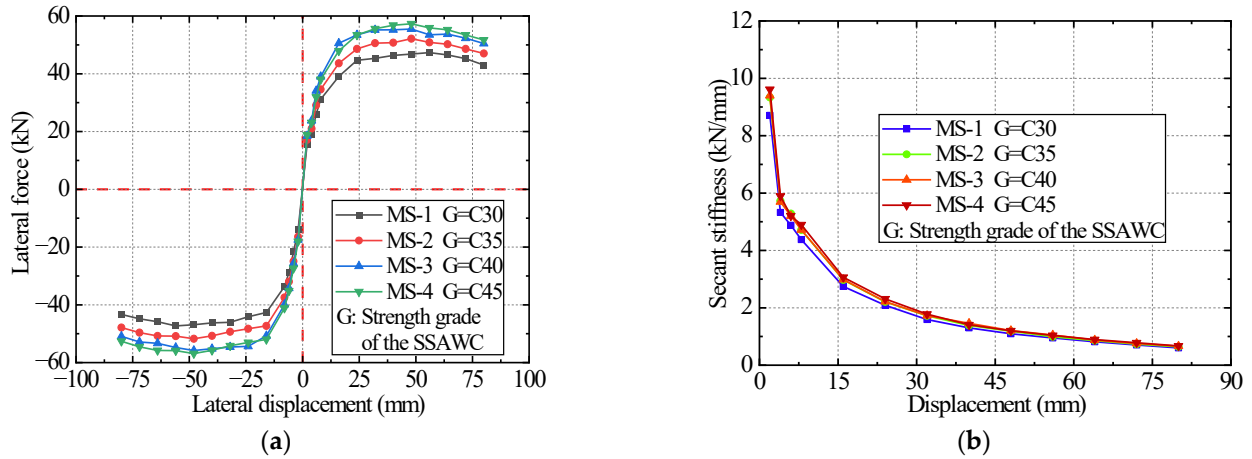


Figure 24. Comparison of the skeleton and stiffness degradation curves for numerical models with different SSAWC strengths. (a) Skeleton curves of MS-1 to MS-4; (b) Stiffness degradation curves of MS-1 to MS-4.

(4) Influence of SSAWC self-stress on the strengthening effect

As the self-stress value increased from 0 to 2.8 MPa, the initial stiffness, peak load, ductility coefficient, and secant stiffness of the pier column increased by 34.47%, 37.96%, 30.35%, and 23.33%, respectively (Table 8 and Figure 25). We inferred that an increase in the initial self-stress could significantly enhance the confinement effect of the filling layer on the core pier column. The column was placed in a triaxial compression state to improve its stiffness, bearing capacity, and ductility. However, when the self-stress value of the filled concrete increased from 2.2 to 2.8 MPa, the peak load growth rate decreased from 12.57% to 9.08%, the ductility coefficient growth rate decreased from 5.88% to 1.57%, and the pier column ultimate load began to decrease, indicating that excessive self-stress (i.e., >2.2 MPa) provided limited improvement on the seismic performance of the pier columns. Therefore, under the premise of meeting the strengthened pier columns’ bearing capacity design requirements, the initial self-stress value of the filled concrete should not exceed 2.2 MPa.

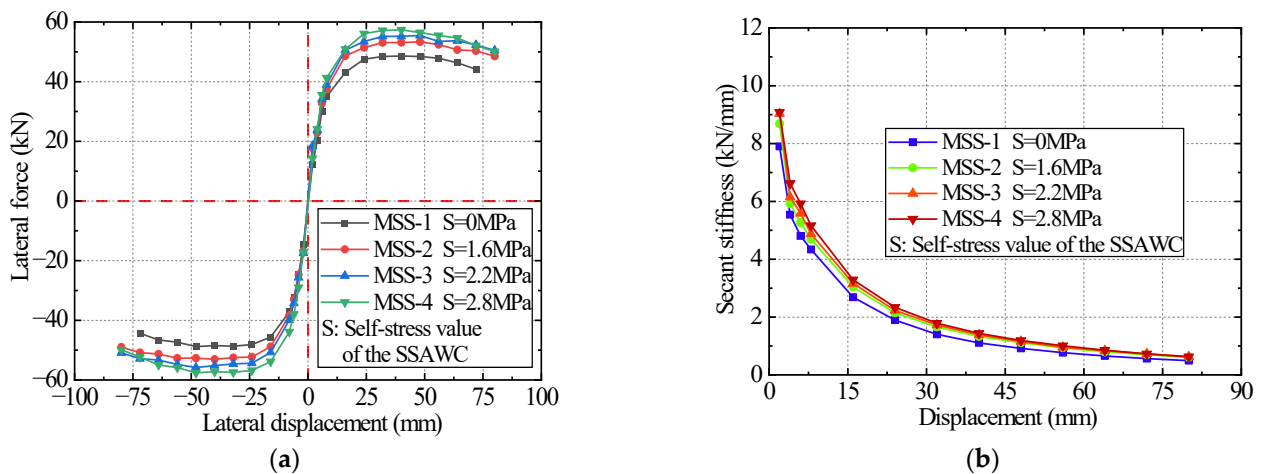


Figure 25. Comparison of the skeleton and stiffness degradation curves for numerical models with different self-stresses. (a) Skeleton curves of MSS-1 to MSS-4; (b) Stiffness degradation curves of MSS-1 to MSS-4.

(5) Influence of axial compression ratio on the strengthening effect

As the axial compression ratio increased from 0.1 to 0.4, the initial stiffness and ductility coefficient of the pier column first increased and then decreased (Table 8); the peak load increased by 18% during this process. The ductility coefficient and initial stiffness reached their respective maximum values of 7.25 and 17.98 kN/mm when the axial compression ratio was 0.2 and 0.3, respectively. We inferred that an increase in the axial compression ratio could delay the tensile steel rebar yield and tensile concrete cracking to a certain extent, improving the pier column's overall stiffness and bearing capacity. However, when the axial compression ratio of the pier column increased from 0.3 to 0.4, the initial stiffness and ultimate load decreased, the ductility coefficient decreased by 15.44%, the growth rate of the peak load decreased from 4.44% to 3.43%, and the increase in secant stiffness was relatively small (Figure 26). Accordingly, we conclude that an excessively high axial compression ratio (i.e., >0.3) can accelerate the crushing and spalling of concrete in the compression zone and easily produce an additional bending moment with a large horizontal displacement, resulting in a decrease in the ductility and ultimate load, further accelerating the failure damage of the pier column. Therefore, the axial compression ratio of the pier columns should not exceed 0.3.

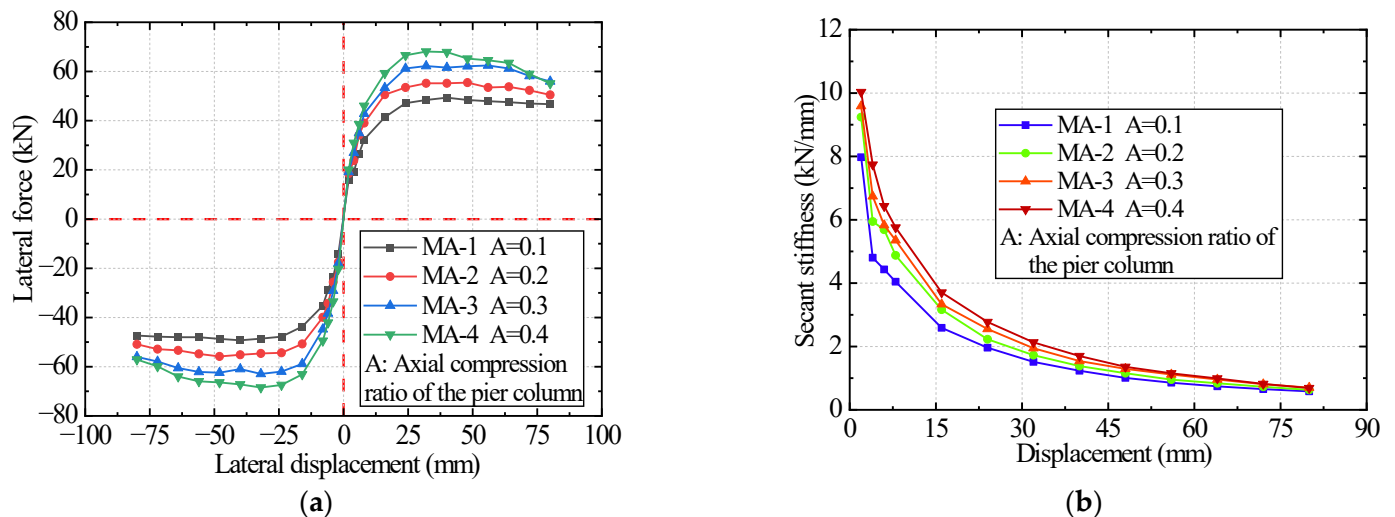


Figure 26. Comparison of the skeleton and stiffness degradation curves for numerical models with different axial compression ratios. (a) Skeleton curves of MA-1 to MA-4; (b) Stiffness degradation curves of MA-1 to MA-4.

5. Restoring Force Model

The restoring force model is a practical mathematical model obtained by appropriate abstraction and simplification based on the relationship between the force and displacement of a structure or component under cyclic loading action. It reflects the accurate constitutive relationship of the material or section and the mechanical characteristics of the structure or component at each moment during the loading process. It is also the basis for analyzing the elastic–plastic responses of structures. An ideal restoring force model can better reflect the hysteretic characteristics of components regarding strength, stiffness, energy dissipation, and ductility and can simplify the calculation by ensuring the accuracy and reliability of the calculation results.

The restoring force model comprises the skeleton curve model and the hysteresis rule. The skeleton curve model determines the characteristic points of the restoring force model, such as the cracking, yield, peak, and ultimate points. The hysteresis rule specifies the track route during the positive and negative loading and unloading process, as well as characteristics such as strength degradation and stiffness degradation. There are two types of restoring force models: curvilinear and broken line. The stiffness of curvilinear models

changes continuously, and the calculated results are close to the actual situation, whereas its calculation method and stiffness determination are more complicated. In contrast, the broken line restoring force model is simpler and more practical, whereas the stiffness change is discontinuous owing to the existence of inflection points on the curve; therefore, the accuracy of the calculation results requires further verification and improvement. Recently, many scholars such as Deng [69], Ma [70], Han [73], and Zhang [74] proposed restoring force models of concrete-filled steel tubular columns under different working conditions through experimental and numerical simulation studies. In this study, the restoring force model of a pier column strengthened using the IPCSAM was established based on the results of the quasi-static test and extended parameter analysis.

5.1. Skeleton Curve Model

5.1.1. Skeleton Curve Model Establishment

Considering the difficulty associated with observing concrete cracking inside the strengthened pier column during the loading process and accurately providing information on the cracking point of the strengthened pier column, a trilinear model was adopted (Figure 27). This model was then applied to establish the skeleton curve model of the strengthened pier column using the IPCSAM; the first three characteristic points, A (yield point), B (peak point), and C (ultimate point), were required. Each characteristic point could be expressed by the corresponding load, displacement, and stiffness, determined through regression fitting of the quasi-static test and the extended parameter analysis results; the total number of specimens used for regression was 25.

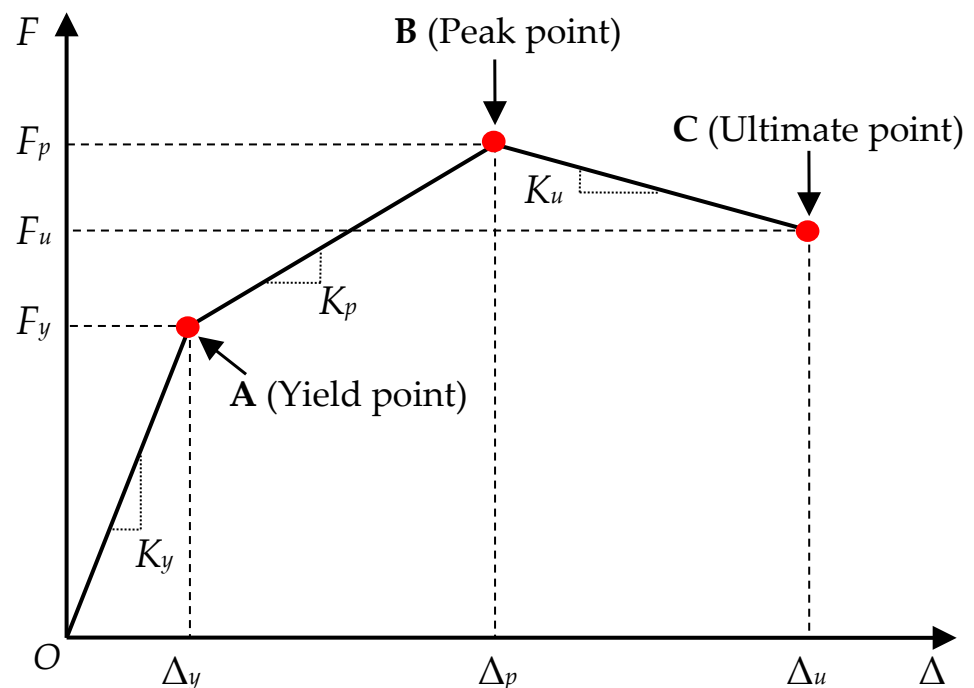


Figure 27. Trilinear skeleton curve model.

Calculation of Yield Point

(1) Yield Load

According to the quasi-static test and extended parameter analysis results, the ratio of peak load to yield load decreases with increased segment thickness, length–diameter ratio, axial compression ratio, and filled concrete strength, and increases with an increased

reinforcement ratio of the filled concrete and initial self-stress. Accordingly, and considering previous studies [71,72], Equation (5) was obtained:

$$\frac{F_p}{F_y} = A - k_1 k_2 B n + C \rho_v - k_3 D f_c + E m - F \lambda - G u \tag{5}$$

where F_y and F_p are the yield and ultimate loads, respectively; n represents the ratio of the segment thickness to the filling-layer thickness; ρ_v represents the reinforcement ratio of the filling layer; f_c represents the ratio of the filled concrete strength to the C40 concrete strength; m is the initial self-stress of filled concrete; λ and u represent the length–diameter ratio and axial compression ratio of the pier column, respectively. Parameters A–E are regression coefficients; k_1 , k_2 , and k_3 represent the adjustment coefficients of the concrete strength of the segment, reinforcement ratio of the segment, and increased area of the filling layer, respectively, which can be calculated using Equations (6)–(8):

$$k_1 = 1 + \left(\frac{f_s}{40} - 1 \right) \times 0.16 \tag{6}$$

$$k_2 = 1 + \left(\frac{\rho_s}{0.5} - 1 \right) \times 0.08 \tag{7}$$

$$k_3 = 1 + \left(\frac{h_s}{d_s} - 0.1 \right) \times 0.8 \tag{8}$$

where f_s and ρ_s represent the concrete strength and the reinforcement ratio of the segment, respectively; h_s is the thickness of the filling layer; d_s is the diameter of the strengthened pier column.

The relationship between the peak and yield loads, expressed as a multiple linear equation, was obtained by linear regression fitting, as follows:

$$\frac{F_p}{F_y} = 1.53 - 0.81n + 0.08\rho_v - 0.16f_c + 0.02m - 0.01\lambda - 0.12u \tag{9}$$

The significance test process of the regression represented by Equation (9) at the inspection level of $\alpha = 0.05$ is as follows: $F = 4.15 > F_{0.05}(6, 18) = 2.66$, indicating that the regression equation was significant and reliable at a 95% confidence level.

(2) Yield Displacement

The yield displacement Δ_y of the strengthened pier column consists primarily of the bending deformation Δ_{by} and shear deformation Δ_{sy} , expressed as

$$\Delta_y = \Delta_{by} + \Delta_{sy} \tag{10}$$

Δ_{by} and Δ_{sy} are expressed as

$$\Delta_{by} = \frac{1}{3} \phi_y L^2 \tag{11}$$

$$\Delta_{sy} = 1.2 \frac{F_y L}{G d_w^2} \tag{12}$$

where L is the effective calculated height of the strengthened pier column; G represents the shear modulus of the concrete of the column body, which can be set to 0.4 times the elastic modulus; d_w represents the diameter of the plastic hinge region, considered as the diameter of the unreinforced core pier column; ϕ_y represents the yielding curvature, calculated using Equation (13). According to a previous study [75], parameter β was obtained through

linear regression fitting based on the results of the quasi-static test and extended parameter analysis, as presented in Equation (14):

$$\phi_y = \beta \frac{f_y}{E_s d_w} \tag{13}$$

$$\beta = 1 - 3.37n + 1.04\rho_v - 0.33f_c + 0.15m + 0.28\lambda + 1.05u \tag{14}$$

where f_y represents the design value of the rebar compressive strength; E_s represents the elastic modulus of the rebar.

The significance test process of the regression Equation (14) at the inspection level of $\alpha = 0.05$ is as follows: $F = 21.11 > F_{0.05}(6, 18) = 2.66$, indicating that the regression equation was significant and reliable at a 95% confidence level.

(3) Yield Stiffness

After determining the yield load F_y and yield displacement Δ_y , the slope of the line connecting origin O and yield point A represents the yield stiffness K_y , which is expressed as follows:

$$K_y = \frac{F_y}{\Delta_y} \tag{15}$$

Calculation of Peak Point

(1) Peak Load

According to the Chinese “Code for design of strengthening concrete structure” [55] and other studies [76,77], the proposed equation for the peak load F_p (i.e., lateral bearing capacity) is

$$F_p = \frac{3}{4}\pi r^2 f_{t1} + \frac{3}{4}\gamma_1 f_{t2} A_{sc} + \frac{\pi A_{sv1} f_{yv1}}{2s_1} \cdot D_1 \cdot \sin \alpha_1 + \gamma_2 \frac{\pi A_{sv2} f_{yv2}}{2s_2} \cdot D_2 \cdot \sin \alpha_2 \tag{16}$$

where r represents the section radius of the core-pier column; A_{sc} represents the cross-sectional area of the filling layer; f_{t1} and f_{t2} represent the design values of the axial tensile strength for the concrete of the core pier column and the filled concrete, respectively; A_{sv1} and A_{sv2} represent the cross-sectional areas of a single stirrup in the core pier column and the filled concrete, respectively; f_{yv1} and f_{yv2} represent the design values of the tensile strengths of the stirrups in the core pier column and the filled concrete, respectively; s_1 and s_2 represent the spacings of the stirrups in the core pier column and filled concrete, respectively; D_1 and D_2 represent the circumferential diameters enclosed by the centerline of the stirrup in the core pier column and filled concrete, respectively; α_1 and α_2 represent the angles between the stirrup and the centerline of the annular cross-section in the core pier column and the filled concrete, respectively; γ_1 and γ_2 represent the strength utilization coefficient of the concrete and stirrups in the filling layer, respectively, obtained through linear regression fitting, as presented in Equations (17) and (18).

$$\gamma_1 = 1.53 + 0.84n - 0.6f_c \tag{17}$$

$$\gamma_2 = 0.86 + 0.39\rho_v \tag{18}$$

As the connection between the segments cannot form an entire shell with LCSS, similar to a steel tube, the peak bearing capacity of the LCSS is lower than that of the core pier column and filled concrete. Thus, the contribution of the LCSS was not considered in the calculation of the peak force. The significance test processes of the regression equations at the inspection level of $\alpha = 0.05$ are as follows: for Equation (17), $F = 5.03 > F_{0.05}(2, 22) = 3.44$, and for Equation (18), $F = 7.15 > F_{0.05}(1, 23) = 4.28$, indicating that the regression equations were significant and reliable at a 95% confidence level.

(2) Peak Displacement

According to the quasi-static test and extended parameter analysis results, the ratio of peak displacement to yield displacement decreases with increased segment thickness, length–diameter ratio, axial compression ratio, filled concrete strength, and the reinforcement ratio of the filled concrete while increasing with an increase in the initial self-stress. Thus, the ratio of peak displacement Δ_p to yield displacement Δ_y is expressed by Equation (19) through linear regression fitting as follows:

$$\frac{\Delta_p}{\Delta_y} = 9.36 - 5.53n - 1.17\rho_v - 1.19f_c - 0.23m + 0.29\lambda - 3.16u \quad (19)$$

The significance test process of this regression equation at the inspection level of $\alpha = 0.05$ is as follows: $F = 4.40 > F_{0.05}(6, 18) = 2.66$, indicating that the regression equation was significant and reliable.

(3) Peak Stiffness

After determining the peak load F_p and peak displacement Δ_p , the slope of the line connecting peak point B and yield point A represents the peak stiffness K_p , which is expressed as Equation (20):

$$K_p = \frac{F_p - F_y}{\Delta_p - \Delta_y} \quad (20)$$

Calculation of Ultimate Point

(1) Ultimate Load

According to the Chinese code [62], loading can be stopped when the horizontal load decreases to 85% of the peak load. Thus, the ultimate load F_u was set as 85% of the peak load F_p , as expressed in Equation (21):

$$F_u = 0.85F_p \quad (21)$$

(2) Ultimate Displacement

Similar to Equation (19), the ratio of ultimate displacement Δ_u to yield displacement Δ_y is expressed by Equation (22) through linear regression fitting:

$$\frac{\Delta_u}{\Delta_y} = 6.11 + 1.21n + 0.75\rho_v + 1.62f_c - 0.23m - 0.18\lambda - 3.33u \quad (22)$$

The significance test at the inspection level of $\alpha = 0.05$ is expressed as follows: $F = 2.88 > F_{0.05}(6, 18) = 2.66$, indicating that the regression Equation (22) was significant and reliable.

(3) Ultimate Stiffness

After determining the ultimate load F_u and ultimate displacement Δ_u , the slope of the line connecting the ultimate point C and peak point B represents the ultimate stiffness K_u , which is expressed as

$$K_u = \frac{F_u - F_p}{\Delta_u - \Delta_p} \quad (23)$$

5.1.2. Skeleton Curve Model Verification

The accuracy and reliability of the skeleton curve model were verified by comparing the experimentally measured and theoretically calculated values for each characteristic point of the five strengthened specimens: RP-0, RP-1, RP-2, RP-4, and RP-5. Since the initial damage to the pier column was not considered during the establishment of the skeleton curve model, strengthened specimen RP-3 was not selected for model verification.

As shown in Tables 9–11, the relative errors between the measured and calculated values of the characteristic points for each strengthened specimen were within 10%, and 5/30 groups from the contrast data had an error > 5%. Moreover, the theoretically calculated skeleton curve models of each strengthened specimen agreed well with the skeleton curves measured in the quasi-static test (Figure 28). The primary causes of the apparent deviation after the yield point between the measured and calculated models under reverse loading are the asymmetry of the skeleton curve caused by the asymmetry of the specimen loading and damage, as well as the discreteness of the material (Figure 28b,d,e). Therefore, the skeleton curve model obtained using the proposed calculation method for the characteristic points can accurately reflect changes in the bearing capacity, deformation, and stiffness of the pier column strengthened using the IPCSAM under horizontal cyclic loading.

Table 9. Calculated and measured strengthened specimens' yield points.

Specimen	Yield Load			Yield Displacement		
	$F_{y,m}$ (kN)	$F_{y,c}$ (kN)	RE (%)	$\Delta_{y,m}$ (mm)	$\Delta_{y,c}$ (mm)	RE (%)
RP-0	38.46	37.05	3.67	9.56	9.28	2.93
RP-1	45.25	42.18	6.78	9.11	9.47	3.95
RP-2	41.28	40.32	2.33	9.36	9.65	3.10
RP-4	30.38	29.20	3.88	13.06	12.59	3.60
RP-5	20.48	20.91	2.10	20.67	19.75	4.45

Note: (a) $F_{y,m}$ and $F_{y,c}$ represent the measured and calculated yield load, respectively. (b) $\Delta_{y,m}$ and $\Delta_{y,c}$ represent the measured and calculated yield displacement, respectively. (c) RE represents the relative error, calculated as $RE = (F_{y,c} - F_{y,m})/F_{y,m} \times 100\%$ or $RE = (\Delta_{y,c} - \Delta_{y,m})/\Delta_{y,m} \times 100\%$.

Table 10. Calculated and measured strengthened specimens' peak points.

Specimen	Peak Load			Peak Displacement		
	$F_{p,m}$ (kN)	$F_{p,c}$ (kN)	RE (%)	$\Delta_{p,m}$ (mm)	$\Delta_{p,c}$ (mm)	RE (%)
RP-0	48.16	46.32	3.82	31.59	29.70	5.98
RP-1	56.48	53.92	4.53	23.53	25.00	6.25
RP-2	51.46	52.62	2.25	22.82	21.15	7.32
RP-4	37.62	38.96	3.56	27.37	26.66	2.59
RP-5	26.09	25.38	2.72	53.66	51.19	4.60

Note: (a) $F_{p,m}$ and $F_{p,c}$ represent the measured and calculated peak load, respectively. (b) $\Delta_{p,m}$ and $\Delta_{p,c}$ represent the measured and calculated peak displacement, respectively. (c) RE represents the relative error, calculated as $RE = (F_{p,c} - F_{p,m})/F_{p,m} \times 100\%$ or $RE = (\Delta_{p,c} - \Delta_{p,m})/\Delta_{p,m} \times 100\%$.

Table 11. Calculated and measured strengthened specimens' ultimate points.

Specimen	Ultimate Load			Ultimate Displacement		
	$F_{u,m}$ (kN)	$F_{u,c}$ (kN)	RE (%)	$\Delta_{u,m}$ (mm)	$\Delta_{u,c}$ (mm)	RE (%)
RP-0	40.93	39.37	3.81	56.02	57.98	3.50
RP-1	48.01	45.83	4.54	76.58	73.70	3.76
RP-2	43.74	44.73	2.26	64.37	67.19	4.38
RP-4	31.97	33.12	3.60	95.70	89.57	6.41
RP-5	22.18	21.57	2.75	123.61	119.92	2.99

Note: (a) $F_{u,m}$ and $F_{u,c}$ represent the measured and calculated ultimate load, respectively. (b) $\Delta_{u,m}$ and $\Delta_{u,c}$ represent the measured and calculated ultimate displacement, respectively. (c) RE represents the relative error, calculated as $RE = (F_{u,c} - F_{u,m})/F_{u,m} \times 100\%$ or $RE = (\Delta_{u,c} - \Delta_{u,m})/\Delta_{u,m} \times 100\%$.

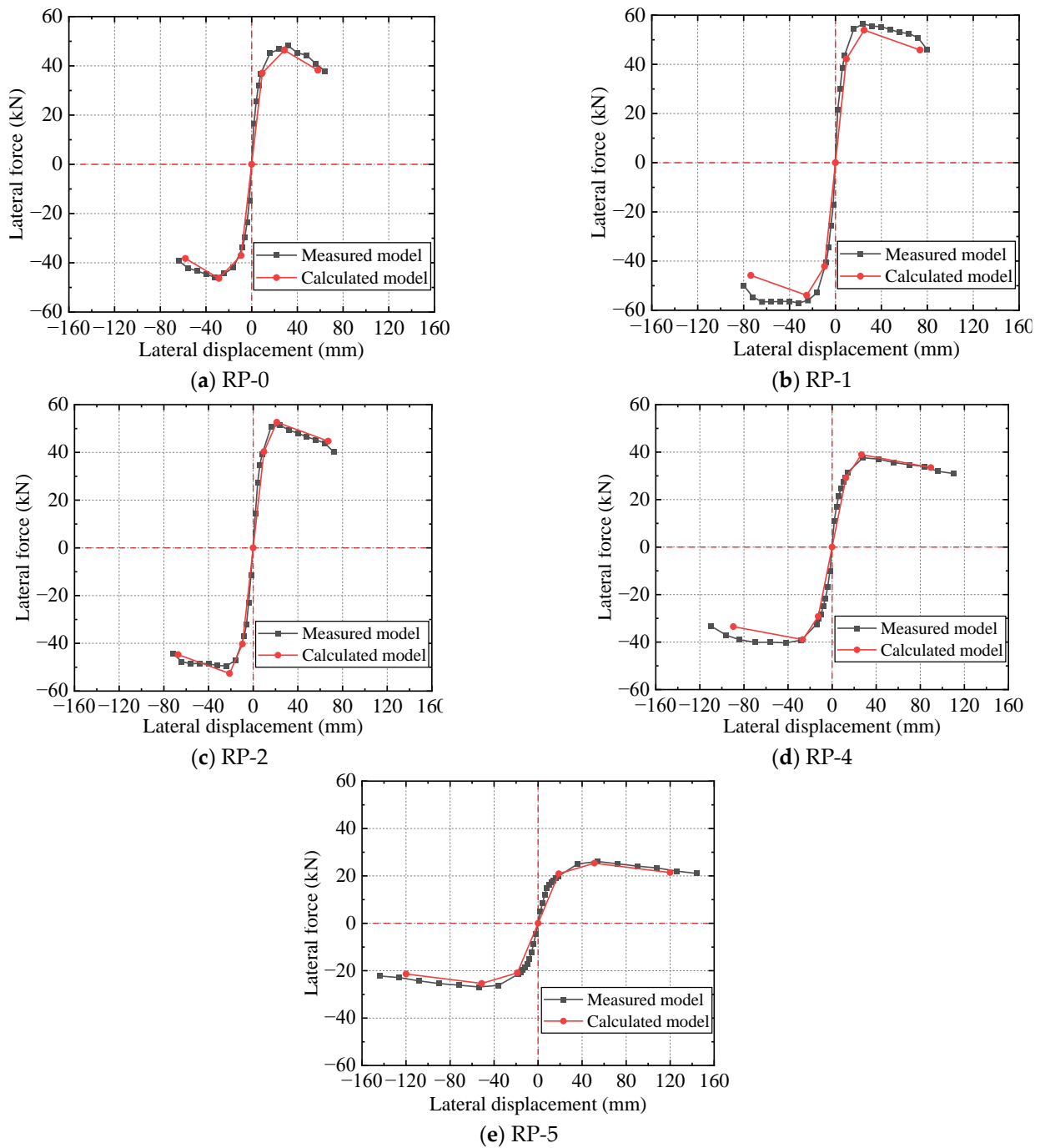


Figure 28. Comparison of the theoretical calculated and experimental measured skeleton curve models of the strengthened specimens (a–e).

5.2. Hysteresis Curve Model

5.2.1. Hysteresis Rule and Model

A hysteresis rule is required to describe the hysteresis behavior of a pier column strengthened using the IPCSAM under horizontal cyclic loading. The hysteresis behavior is described through numerous rules for unloading and reloading; hence, establishing a restoring force model of strengthened specimens under cyclic loading requires determining forward and reverse loading and unloading paths, i.e., the hysteresis rule. The typical hysteresis rules, as presented in Figure 29, define the hysteresis behavior as follows:

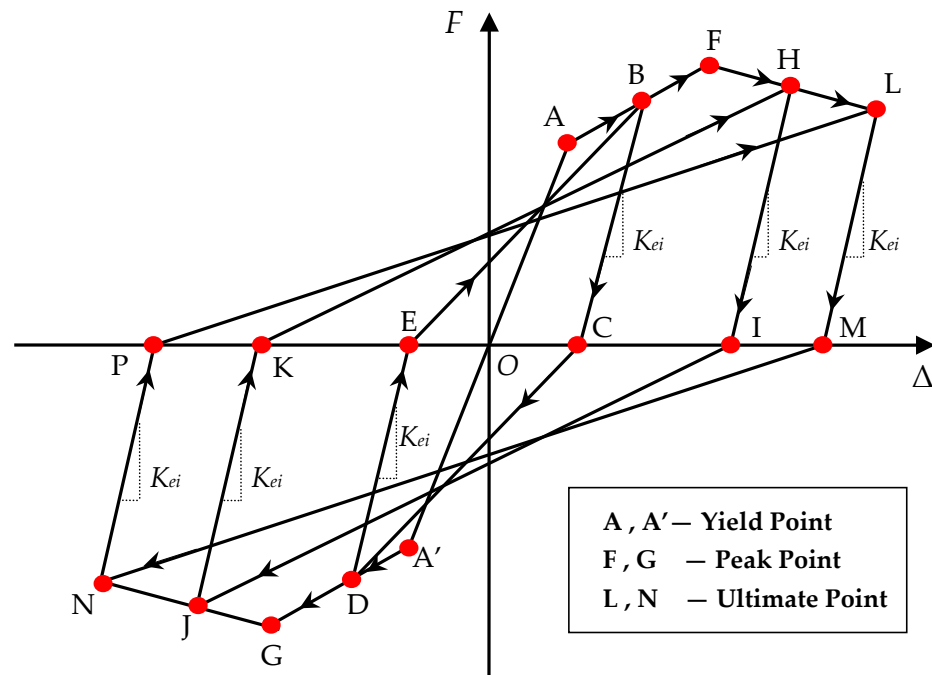


Figure 29. Definition of hysteresis rules for the restoring force model.

(a) The stage before loading to yield point A. At this point, the strengthened specimens are primarily in the elastic stage with no residual deformation. The loading and unloading paths follow the elastic section of the skeleton curve. Thus, the loading and unloading stiffnesses at this stage can be considered as the yield stiffness K_y , calculated using Equation (15). The loading path is as follows: $O \rightarrow A \rightarrow O \rightarrow A' \rightarrow O$.

(b) The stage where the load exceeds the yield point A but does not reach the peak point F. First, the origin point O is loaded to a certain point B according to the skeleton curve, and the peak stiffness K_p of segment AB can be calculated using Equation (20). Because stiffness degradation occurs during unloading in this stage, point B can be unloaded to point C according to the unloading stiffness K_{ei} and reversely loaded to point D, which is polarly symmetric to point B in the skeleton curve. The loading stiffness of segment CD is its slope. Subsequently, point D is reversely unloaded to point E, according to K_{ei} , and finally loaded to point B. The loading path is as follows: $O \rightarrow A \rightarrow B \rightarrow C \rightarrow D \rightarrow E \rightarrow B$. According to Ma et al. [70], the unloading stiffness K_{ei} can be calculated using Equation (24), where Δ_i represents the displacement at the i -th unloading point. Both α and ω are adjustment coefficients calculated using Equation (25) and Equation (26), respectively. The significance test processes of the regression equations at the inspection level of $\alpha = 0.05$ are as follows: for Equation (25), $F = 3.68 > F_{0.05}(6, 18) = 2.66$, and for Equation (26), $F = 3.95 > F_{0.05}(6, 18) = 2.66$, indicating that the regression equations were significant and reliable at a 95% confidence level.

$$K_{ei}/K_y = \alpha(\Delta_i/\Delta_y)^\omega \tag{24}$$

$$\alpha = 5.39 + 6.62n - 0.89\rho_v - 0.48f_c + 0.21m - 0.71\lambda + 5.63u \tag{25}$$

$$\omega = -2.26 - 0.81n + 0.13\rho_v - 0.16f_c - 0.01m + 0.29\lambda - 0.26u \tag{26}$$

(c) The loading stage from peak point F to ultimate point L. The hysteresis change and stiffness degradation during loading and unloading are similar to those in the last stage. The ultimate stiffness K_u of the FH segment can be calculated using Equation (23), and the unloading stiffness K_{ei} can be calculated using Equations (24)–(26). The loading path is as follows: $O \rightarrow A \rightarrow B \rightarrow F \rightarrow H \rightarrow I \rightarrow J \rightarrow K \rightarrow H \rightarrow L \rightarrow M \rightarrow N \rightarrow P \rightarrow L$.

5.2.2. Hysteresis Curve Model Verification

According to the hysteresis rules proposed in Section 5.2.1, the calculated hysteresis curve models of the five strengthened specimens RP-0, RP-1, RP-2, RP-4, and RP-5 were established and compared with the experimentally measured hysteresis curves. A certain error existed in the initial stiffness between the measured and calculated hysteresis curve models (Figure 30). This is primarily due to the adopted trilinear model ignoring the cracking point (i.e., elasticity limit) before yielding the strengthened pier column. The initial stiffness of the calculated model is taken as the slope of the line connecting the yield point and the origin, which degrades after the pier column cracks. Therefore, the initial stiffness of the measured hysteresis curve models was slightly higher than that of the calculated models. A slight deviation occurred after the yield stage between the measured and calculated hysteresis curve models; however, the models were in basic agreement. Thus, the hysteresis curve model and the hysteresis rules proposed in Section 5.2.1 can relatively accurately and reasonably reflect the hysteresis characteristics of the specimens strengthened using the IPCSAM. In addition, the proposed restoring force model has good applicability as a reference for practical seismic strengthening pier designs.

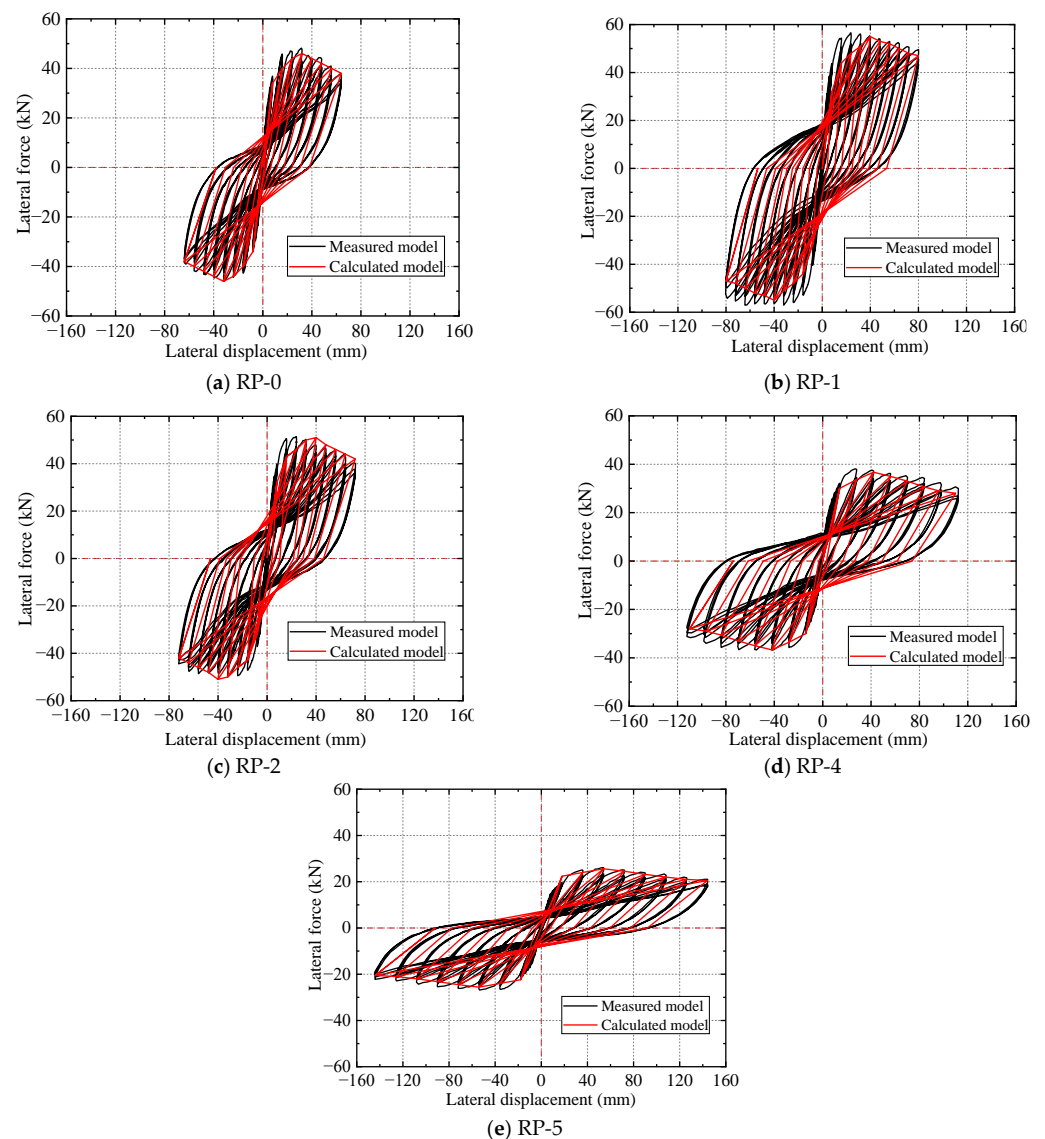


Figure 30. Comparison of the theoretical and experimental hysteresis curve models for the strengthened specimens (a–e).

6. Conclusions

This study explored the impacts of different influencing factors on the seismic performance of underwater concrete piers strengthened using the IPCSAM through a quasi-static test and extended parameter analysis. A restoring force model for strengthened piers was ultimately established, and the following conclusions were drawn.

- (1) As an undrained strengthening technique, the proposed IPCSAM exhibits good seismic strengthening effects on underwater concrete piers. Compared with the unreinforced pier columns, the peak load, ductility coefficient, and initial stiffness of the specimens strengthened using the IPCSAM increased by approximately 83.5–106.4%, 16.3–50.2%, and 83.9–177.3%, respectively, while significantly improving the secant stiffness, energy dissipation per cycle, and equivalent viscous damping. In addition, the bearing capacity, stiffness, and energy dissipation capacity of the strengthened specimen with initial damage could be improved to a near-undamaged state, excluding the ductility.
- (2) As a filling material, SSAWC can improve the seismic performance of strengthened specimens. The initial self-stress produced by the SSAWC can provide a circumferential preloading effect on the core pier column to improve its bearing, stiffness, energy dissipation, and deformation capacities. Compared with the specimen using AWC, the peak load, ductility coefficient, and initial stiffness of the specimen with a self-stress value of 1.6 MPa increased by 17.3%, 43.5%, and 8.3%, respectively. Moreover, the secant stiffness, energy dissipation per cycle, and equivalent viscous damping were improved. In addition, under the premise of satisfying the bearing capacity design requirements, the self-stress value of the SSAWC should not exceed 2.2 MPa, the strength grade of the SSAWC should be 1–2 grades higher than the concrete strength grade of the core pier column, and the SSAWC should adopt the constructional reinforcement ratio.
- (3) The LCSS exhibited reliable connection performance and strength in the quasi-static test and remained intact and confined when the specimen was damaged. An increase in the reinforcement ratio of the LCSS from 0.25% to 0.5% increased the peak load, initial stiffness, and ductility coefficient of the strengthened specimen by 9.76%, 16.18%, and 22.24%, respectively. The secant stiffness, energy dissipation per cycle, and equivalent viscous damping were also improved. An appropriate LCSS thickness can effectively improve the seismic performance of strengthened specimens, and the recommended thickness-diameter ratio is 1/10.
- (4) An increase in the length-diameter ratio of a strengthened pier column can significantly reduce its seismic performance. An appropriate axial compression ratio can improve the bearing capacity, stiffness, ductility, and energy dissipation capacity of strengthened pier columns, and the axial compression ratio should not exceed 0.3.
- (5) The proposed restoring force model of pier columns strengthened using the IPCSAM has good applicability and can accurately reflect the hysteresis characteristics of the strengthened specimens. For the skeleton curve model, the relative errors between the measured and calculated values of the characteristic points for each strengthened specimen were within 10%, and only 5 of 30 groups of contrast data had an error exceeding 5%. A certain error existed in the initial stiffness between the measured and calculated hysteresis curve models, and the deviation after the yield stage was small.

The IPCSAM adopted in this study is an undrained strengthening method with economical, efficient, and shipping traffic-friendly benefits. Moreover, applying SSAWC self-stress and the LCSS constraint can effectively improve the seismic performance of strengthened piers. Additionally, for design engineers, the reasonable self-stress value, strength grade, and reinforcement ratio of the SSAWC, the reasonable ratio of the LCSS thickness to pier column diameter, and the established restoring force model proposed in this study can provide a basis and reference for the seismic strengthening design of underwater damaged piers in practical engineering.

In future research, the interfacial bonding performance between the filled concrete and adjacent members, the durability of the segment sleeves, and the modular design of the filled concrete and segment sleeves should be further explored. Moreover, additional experimental data and numerical simulations are required to validate the proposed restoring force model for piers strengthened using IPCSAM.

Author Contributions: Conceptualization, S.S. and Y.S.; methodology, Y.S.; software, W.X. and Y.S.; validation, Y.S.; formal analysis, Y.S.; investigation, Y.S.; resources, S.S.; data curation, Y.S. and W.X.; writing—original draft preparation, Y.S.; writing—review and editing, S.S.; visualization, Y.S.; supervision, S.S.; project administration, S.S.; funding acquisition, S.S. All authors have read and agreed to the published version of the manuscript.

Funding: This work was funded by the National 13th Five-Year Research Program of China (Grant No. 2016YFC0700706), Traffic Science and Technology Project of Fujian Communication Department, China (Grant No. 201536 and 201716), and the Education and Scientific Research Project for Young and Middle-aged Teachers of Fujian Province, China (Grant No. JAT60044).

Institutional Review Board Statement: Not applicable.

Informed Consent Statement: Not applicable.

Data Availability Statement: The data presented in this study are available on request from the corresponding author. The data are not publicly available due to the funding contract.

Acknowledgments: Wansong Xu assisted with the experiments as well as numerical analysis. The authors express their gratitude to the anonymous reviewers for their constructive comments and suggestions.

Conflicts of Interest: Author Yu Sun was employed by the company Shanghai Construction Decoration Engineering Group Co., Ltd. and Author Wansong Xu was employed by the company East China Electric Power Design Institute Co., Ltd. of China Power Engineering Consulting Group. The remaining authors declare that the research was conducted in the absence of any commercial or financial relationships that could be construed as a potential conflict of interest.

References

1. Wu, S.F.; Jiang, S.F.; Shen, S.; Wu, Z.Q. The Mix Ratio Study of Self-Stressed Anti-Washout Underwater Concrete Used in Non-drainage Strengthening. *Materials* **2019**, *12*, 324. [[CrossRef](#)]
2. Wu, S.F.; Ge, Y.J.; Jiang, S.F.; Shen, S.; Zhang, H. Experimental Study on the Axial Compression Performance of an Underwater Concrete Pier Strengthened by Self-Stressed Anti-Washout Concrete and Segments. *Materials* **2021**, *14*, 6567. [[CrossRef](#)] [[PubMed](#)]
3. Su, J.S.; Wu, D.Q.; Wang, X.W. Influence of ground motion duration on seismic behavior of RC bridge piers: The role of low-cycle fatigue damage of reinforcing bars. *Eng. Struct.* **2023**, *279*, 115587. [[CrossRef](#)]
4. Dawn, E.L.; Sharon, E.G.; Adrian, M.N.; Jack, P.M. Repair of Earthquake-Damaged Bridge Columns. *Struct. J.* **2001**, *98*, 233–242.
5. Zheng, S.K. RC Columns Increased Section Method Based on the Concept of Confined Concrete. Master's Thesis, Chongqing University, Chongqing, China, 2010. (In Chinese)
6. Ren, W.; Lesley, H.S.; Gai, Y.T.; Kang, X. Test Results and Nonlinear Analysis of RC T-beams Strengthening by Bonded Steel Plates. *Int. J. Concr. Struct. Mater.* **2015**, *9*, 133–143. [[CrossRef](#)]
7. Yang, S.Y. Experimental Research on Seismic Behavior of RC Bridge Piers Combination Strengthened by FRP Bars and FRP Sheets. Master's Thesis, Southeast University, Nanjing, China, 2012. (In Chinese)
8. Tomii, M.; Sakino, K.; Xiao, Y.; Watanabe, K. Earthquake Resisting Hysteretic Behavior of Reinforced Concrete Short Columns Confined by Steel Tube. In Proceedings of the International Speciality Conference on Concrete Filled Steel Tubular Structures, Harbin, China, 12–15 August 1985; pp. 119–125. (In Chinese)
9. Youm, K.S.; Lee, H.E.; Choi, S. Seismic performance of repaired RC columns. *Mag. Concr. Res.* **2006**, *58*, 267–276. [[CrossRef](#)]
10. Parghi, A.; Alam, M.S. Seismic behavior of deficient reinforced concrete bridge piers confined with FRP—A fractional factorial analysis. *Eng. Struct.* **2016**, *126*, 531–546. [[CrossRef](#)]
11. Mohamed, H.M.; Afifi, M.Z.; Benmokrane, B. Performance Evaluation of Concrete Columns Reinforced Longitudinally with FRP Bars and Confined with FRP Hoops and Spirals under Axial Load. *J. Bridge Eng.* **2014**, *19*, 04014020. [[CrossRef](#)]
12. Saeed, H.Z.; Khan, Q.U.Z.; Ahmed, A.; Ali, S.M.; Lqbal, M. Experimental and finite element investigation of strengthened LSC bridge piers under Quasi-Static Cyclic Load Test. *Compos. Struct.* **2015**, *131*, 556–564. [[CrossRef](#)]
13. Chang, S.Y.; Li, Y.F.; Loh, C.H. Experimental Study of Seismic Behaviors of As-Built and Carbon Fiber Reinforced Plastics Repaired Reinforced Concrete Bridge Columns. *J. Bridge Eng.* **2004**, *9*, 391–402. [[CrossRef](#)]
14. Wang, Y.S. Experimental Research on Concrete Short Columns Confined by Wire Rope under Axial Compression. Master's Thesis, Harbin Institute of Technology, Harbin, China, 2006. (In Chinese)

15. Saatcioglu, M.; Yalcin, C. External Prestressing Concrete Columns for Improved Seismic Shear Resistance. *J. Struct. Eng.* **2003**, *129*, 1057–1070. [[CrossRef](#)]
16. Li, H. Experiment Study on the Seismic Behavior of RC Short Columns Strengthened with Prestressed Steel Wires. Master's Thesis, Beijing University of Technology, Beijing, China, 2011. (In Chinese)
17. Wu, E.; Jiang, W.; Wang, X.Z.; Zhou, Y. Experimental investigation on reinforced RC column with prestressed double helix FRP strip. *Eur. J. Environ. Civ. Eng.* **2013**, *17*, 53–64. [[CrossRef](#)]
18. Fakharifar, M.; Chen, G.; Wu, C.L.; Shamsabadi, A. Rapid Repair of Earthquake-Damaged RC Columns with Prestressed Steel Jackets. *J. Bridge Eng.* **2016**, *21*, 04015075. [[CrossRef](#)]
19. Fatmir, M.; Hadi, B. *Rehabilitation of Deteriorated Timber Piles with Fiber Reinforced Polymer Composites—IABSE Symposium Report*; International Association for Bridge and Structural Engineering: Vancouver, BC, Canada, 2017; pp. 381–388.
20. Hafizah, N.A.K.; Bhutta, M.A.R.; Jamaludin, M.Y.; Warid, M.H.; Iamail, M.; Rahman, M.S.; Yunus, I.; Azman, M. Kenaf Fiber Reinforced Polymer Composites for Strengthening RC Beams. *J. Adv. Concr. Technol.* **2014**, *12*, 167–177. [[CrossRef](#)]
21. Yi, N.H.; Nam, J.W. Evaluation of material and structural performances of developed Aqua-Advanced-FRP for retrofitting of underwater concrete structural members. *Constr. Build. Mater.* **2010**, *24*, 566–576. [[CrossRef](#)]
22. Sen, R.; Mullins, G. Application of FRP composites for underwater piles repair. *Compos. Part B Eng.* **2007**, *38*, 751–758. [[CrossRef](#)]
23. Tang, Y.; Wu, G.; Sun, Z.Y.; Zhang, Y.F. Seismic Performance of Underwater Bridge Columns Strengthened with Prestressed-Concrete Panels and FRP Reinforcement. *J. Compos. Constr.* **2019**, *23*, 04019019. [[CrossRef](#)]
24. Xia, Z.H.; Lin, L.M.; Zhang, J.H.; Jiang, S.F. Seismic performance of underwater RC bridge piers strengthened with self-compacting concrete-filled BFRP jacket. *Structures* **2022**, *39*, 637–652. [[CrossRef](#)]
25. Zhao, B. The Study on Underwater Pier Reinforcement Technology by Precast Concrete Segment Assembled Quickly. Master's Thesis, Southeast University, Nanjing, China, 2015. (In Chinese)
26. Huang, J.C. The Study on Prefabrication Technology of Reinforced Concrete Shield Segment. Master's Thesis, Tongji University, Shanghai, China, 2007. (In Chinese)
27. Liu, X.; Bai, Y.; Yuan, Y.; Mang, H.A. Experimental investigation of the ultimate bearing capacity of continuously jointed segmental tunnel linings. *Struct. Infrastruct. Eng.* **2016**, *12*, 1364–1379. [[CrossRef](#)]
28. Meng, G.; Gao, B.; Zhou, J.; Cao, G.; Zhang, Q. Experimental investigation of the mechanical behavior of the steel fiber reinforced concrete tunnel segment. *Constr. Build. Mater.* **2016**, *126*, 98–107. [[CrossRef](#)]
29. Qu, X.S.; Liu, Q. Bond strength between steel and self-compacting lower expansion concrete in composite columns. *J. Constr. Steel Res.* **2017**, *139*, 176–187. [[CrossRef](#)]
30. Lu, Y.; Liu, Z.; Li, S.; Li, N. Bond behavior of steel fibers reinforced self-stressing and self-compacting concrete filled steel tube columns. *Constr. Build. Mater.* **2018**, *158*, 894–909. [[CrossRef](#)]
31. Huang, C.K.; Shang, Z.Q.; Zhang, P. Experimental research on self-stressing and self-compacting concrete filled steel tube subjected to eccentric compression load. *J. Dalian Univ. Technol.* **2008**, *48*, 564–569. (In Chinese)
32. Zhao, Z.T. Experimental Research on Self-Compacting and Self-Stressing Concrete-Filled Rectangular Steel Tubular Stub Columns under Axial Compression. Master's Thesis, Inner Mongolia University of Science & Technology, Inner Mongolia, China, 2019. (In Chinese)
33. Wang, H.L.; Guo, F.; Wang, B. Experimental research on the axial compression mechanical performance of BFRP tube expansion concrete short columns. *Build. Struct.* **2016**, *46*, 32–36. (In Chinese)
34. Jia, H.Y.; Li, A.W.; Li, F.G.; Han, C.G. Seismic Performance of Self-compacting Self-stressing Concrete-filled Rectangular Steel Tubular Column. *Bull. Chin. Ceram. Soc.* **2018**, *37*, 1338–1343+1354. (In Chinese)
35. Tang, Y.; Wu, G.; Sun, Z.Y. Numerical Study on Seismic Behavior of Underwater Bridge Columns Strengthened with Prestressed Precast Concrete Panels and Fiber-Reinforced Polymer Reinforcements. *Int. J. Polym. Sci.* **2018**, *2018*, 7438694. [[CrossRef](#)]
36. Deng, Z.C.; Li, H. Seismic Behavior of RC Columns Strengthened with Prestressed Steel Wires. *J. Basic Sci. Eng.* **2014**, *22*, 941–951. (In Chinese)
37. Guo, Z.X.; Zhang, J.; Li, C.L. Seismic strengthening of rectangular RC columns using prestressing steel jackets. *China Civ. Eng. J.* **2009**, *42*, 112–117. (In Chinese)
38. Zhao, M. Study on Strengthened Concrete Column's Bearing Performance by the Method of Enlarging Section. Master's Thesis, Xi'an University of Science and Technology, Xi'an, China, 2009. (In Chinese)
39. Lu, Y.Y.; Yi, S.; Li, B.; Zhang, X.P. Experimental research on seismic performance of circular RC column strengthened with self-compacting concrete filled circular steel tube. *J. Build. Struct.* **2018**, *39*, 65–74. (In Chinese)
40. Quan, S.H.; Zhao, H.L.; Wang, T.C.; Lin, H. Analysis of parameter influence on seismic behavior of reinforced RC columns. *Build. Struct.* **2019**, *49*, 49–53+63. (In Chinese)
41. Memon, M.S.; Sheikh, S.A. Seismic Resistance of Square Concrete Columns Retrofitted with Glass Fiber-Reinforced Polymer. *ACI Struct. J.* **2005**, *102*, 774.
42. Wang, X. Experimental Investigation on the Seismic Behaviors of Severe Earthquake Damaged GFRP Tubed RC Bridge Piers with Wrapped CFRP Sheets. Master's Thesis, Dalian University of Technology, Dalian, China, 2011. (In Chinese)
43. Li, J.B.; Gong, J.X.; Wang, L.C. Seismic behavior of corrosion-damaged reinforced concrete columns strengthened using combined carbon fiber-reinforced polymer and steel jacket. *Constr. Build. Mater.* **2009**, *23*, 2653–2663. [[CrossRef](#)]

44. Zhong, C.Z. Seismic Performance of Concrete Filled Steel Tubular Piers Numerical Simulation and Analysis. Master's Thesis, Guangdong University of Technology, Guangdong, China, 2022. (In Chinese)
45. Wang, C. Seismic Behaviors Analysis of Concrete-Filled Thin-Walled Square Steel Box Piers Based on OpenSees. Master's Thesis, Chang'an University, Xi'an, China, 2014. (In Chinese)
46. Priestley, M.J.N.; Seible, F.; Calvi, G.M. *Seismic Design and Retrofit*; John Wiley & Sons: New York, NY, USA, 1996.
47. Lei, T.; Qian, J.; Liu, C.Q. Application of Damaged Plasticity Model for Concrete. *Struct. Eng.* **2008**, *24*, 22–27. (In Chinese)
48. *GB 50010-2010*; Code for Design of Concrete Structures. China Architecture & Building Press: Beijing, China, 2010. (In Chinese)
49. Zhang, J.; Wang, Q.Y.; Hu, S.Y.; Wang, C.J. Parameters Verification of Concrete Damaged Plastic Model of ABAQUS. *Build. Struct.* **2008**, *38*, 127–130. (In Chinese)
50. Supartono, F.; Sidoroff, F. Anisotropic damage modelling for brittle elastic materials. *Symp. Fr. Pol.* **1984**, *37*, 521–534.
51. Wang, Y.X. Experimental Research on Seismic Behavior of Self-Centering Precast Segmental CFST Bridges Piers with Replaceable Composite Panels. Master's Thesis, Tianjin University, Tianjin, China, 2021. (In Chinese)
52. Chen, L.Y. Study on the Seismic Behavior of Prefabricated ECC Encased CFST Piers. Master's Thesis, Chongqing University, Chongqing, China, 2021. (In Chinese)
53. He, K. Study on the Mechanical Properties of Round-Ended Steel Tube-MPC Composite Structure. Master's Thesis, Harbin Institute of Technology, Harbin, China, 2020. (In Chinese)
54. Nakanishi, K.; Kitada, T.; Nakai, H. Experimental study on ultimate strength and ductility of concrete filled steel columns under strong earthquake. *J. Constr. Steel Res.* **1999**, *51*, 297–319. [[CrossRef](#)]
55. *GB 50367-2013*; Code for Design of Strengthening Concrete Structure. China Architecture & Building Press: Beijing, China, 2013. (In Chinese)
56. *ACI 318-19*; Building Code Requirements for Structural Concrete. American Concrete Institute: Farmington Hills, MI, USA, 2019.
57. *DL/T 5117-2021*; Test Code on Anti-Washout Underwater Concrete. China Electric Power Press: Beijing, China, 2021. (In Chinese)
58. *GB 50936-2014*; Technical Code for Concrete Filled Steel Tubular Structures. China Architecture & Building Press: Beijing, China, 2014. (In Chinese)
59. *AISC/ASCI 360-16*; Specification for Structural Steel Buildings. American Institute of Steel Construction: Chicago, IL, USA, 2016.
60. European Committee for Standardization. *Eurocode 4: Design of Composite Steel and Concrete Structures-Part 1-1: General Rules and Rules for Buildings*; British Standards Institution: London, UK, 2004.
61. Shang, Z.Q. Research on Mechanical Behavior of Self-Stressing and Self-Compacting Concrete Filled Steel Tube Columns. Ph.D. Thesis, Dalian University of Technology, Dalian, China, 2008. (In Chinese)
62. *JGJ/T 101-2015*; Specification for Seismic Test of Buildings. China Architecture & Building Press: Beijing, China, 2015. (In Chinese)
63. *AISC/ASCI 341-10*; Seismic Provisions for Structural Steel Buildings. American Institute of Steel Construction: Chicago, IL, USA, 2010.
64. *IBC-2015*; International Building Code. International Code Council, Inc.: Falls Church, VA, USA, 2015.
65. *ASCE/SEI 7-10*; Minimum Design Loads for Building and Other Structures. American Society of Civil Engineers: Reston, VA, USA, 2010.
66. Feng, P.; Qiang, H.L.; Ye, L.P. Discussion and definition on yield points of materials, members and structures. *Eng. Mech.* **2017**, *34*, 36–46. (In Chinese)
67. Feng, P.; Cheng, S.; Bai, Y.; Ye, L.P. Mechanical behavior of concrete-filled square steel tube with FRP-confined concrete core subjected to axial compression. *Compos. Struct.* **2015**, *123*, 312–324. [[CrossRef](#)]
68. Tazarv, M.; Saiidi, M.S. UHPC-filled duct connections for accelerating bridge construction of RC columns in high seismic zones. *Eng. Struct.* **2015**, *99*, 413–422. [[CrossRef](#)]
69. Deng, Z.C.; Li, J.H. Study on restoring force model of RC corroded columns strengthened with hybrid FRP. *Eng. Mech.* **2011**, *28*, 151–159.
70. Ma, K.Z.; Liang, X.W.; Li, B. Research on the restoring force model of high strength concrete-filled rectangular steel tubular columns. *World Earthq. Eng.* **2011**, *27*, 54–59. (In Chinese)
71. Zhang, W.A. Dynamic Behaviors of Concrete Filled Thin-Walled Steel Tubular Composite Columns. Master's Thesis, Fuzhou University, Fuzhou, China, 2017. (In Chinese)
72. Zhou, X.H.; Yan, B.; Liu, J.P. Axial load behavior of circular tube reinforced concrete columns with different length-diameter ratios. *J. Build. Struct.* **2018**, *39*, 11–21. (In Chinese)
73. Han, L.H.; Tao, Z. Ductility coefficient of concrete filled steel tubular columns with square sections. *Earthq. Eng. Eng. Dyn.* **2000**, *20*, 56–65. (In Chinese)
74. Zhang, S.M.; Liu, J.P.; Wang, Y.Y.; Guo, H.L. Hysteretic behavior of biaxially loaded high strength concrete-filled square hollow section beam-columns. *J. Build. Struct.* **2005**, *26*, 9–18. (In Chinese)
75. Priestley, M.J.N.; Kowalsky, M.J. Aspects of drift and ductility capacity of rectangular cantilever structural walls. *Bull. N. Z. Soc. Earthq. Eng.* **1998**, *31*, 73–85. [[CrossRef](#)]

76. Lu, Z.T.; Shi, P.F.; Zhou, Y.Q. Experimental study on shear bearing capacity of circular and annular reinforced concrete members. *J. Build. Struct.* **1995**, *16*, 13–20. (In Chinese)
77. Liu, T.Y. Calculation of the Shearing Resistance of Concrete Structures with Circular Cross Section. *Anhui Archit.* **2007**, *5*, 70–71. (In Chinese)

Disclaimer/Publisher's Note: The statements, opinions and data contained in all publications are solely those of the individual author(s) and contributor(s) and not of MDPI and/or the editor(s). MDPI and/or the editor(s) disclaim responsibility for any injury to people or property resulting from any ideas, methods, instructions or products referred to in the content.